Mutations in the Heterotopia Gene Eml1/EML1 Severely Disrupt the Formation of Primary Cilia

Ana Uzquiano, Carmen Cifuentes-Diaz, Ammar Jabali, Delfina M Romero, Anne Houllier, Florent Dingli, Camille Maillard, Anne Boland, Jean-François Deleuze, Damarys Loew, et al.

▶ **To cite this version:**

Ana Uzquiano, Carmen Cifuentes-Diaz, Ammar Jabali, Delfina M Romero, Anne Houllier, et al.. Mutations in the Heterotopia Gene Eml1/EML1 Severely Disrupt the Formation of Primary Cilia. Cell Reports, 2019, 28 (6), pp.1596-1611.e10. 10.1016/j.celrep.2019.06.096 . hal-02281812

HAL Id: hal-02281812

https://hal.sorbonne-universite.fr/hal-02281812

Submitted on 9 Sep 2019

HAL is a multi-disciplinary open access archive for the deposit and dissemination of scientific research documents, whether they are published or not. The documents may come from teaching and research institutions in France or abroad, or from public or private research centers.

L'archive ouverte pluridisciplinaire **HAL**, est destinée au dépôt et à la diffusion de documents scientifiques de niveau recherche, publiés ou non, émanant des établissements d'enseignement et de recherche français ou étrangers, des laboratoires publics ou privés.

Article

Cell Reports

Mutations in the Heterotopia Gene *Eml1/EML1* Severely Disrupt the Formation of Primary Cilia

Graphical Abstract

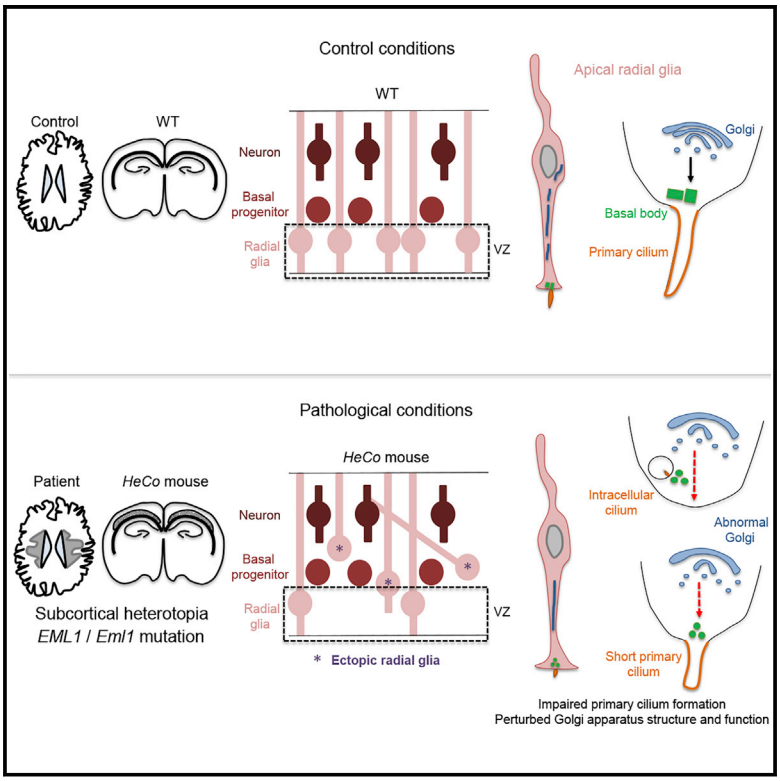

Highlights

- Primary cilium formation is impaired in Eml1/EML1 mutant apical radial glia
- EML1 interacts with RPGRIP1L, a primary cilium protein
- *RPGRIP1L* shows gene variations in a patient with subcortical heterotopia
- Altered Golgi apparatus in Eml1 mutant cells may perturb the Golgi-primary cilium axis

Authors

Ana Uzquiano, Carmen Cifuentes-Diaz, Ammar Jabali, ..., Nadia Bahi-Buisson, Julia Ladewig, Fiona Francis

Correspondence

fiona.francis@inserm.fr

In Brief

Uzquiano et al. show that mutations in *Eml1/EML1*, found in mice and patients with subcortical heterotopia, impair primary cilia formation in apical progenitors. Perturbed anterograde trafficking from the Golgi apparatus seems likely to contribute to this ciliary phenotype. This work uncovers pathological mechanisms potentially triggering the formation of the heterotopia.

Uzquiano et al., 2019, Cell Reports *28*, 1596–1611
August 6, 2019 © 2019 The Authors.
https://doi.org/10.1016/j.celrep.2019.06.096

CellPress

OPEN ACCESS
CellPress

Cell Reports
Article

Mutations in the Heterotopia Gene *Eml1/EML1* Severely Disrupt the Formation of Primary Cilia

Ana Uzquiano,[1,2,3] Carmen Cifuentes-Diaz,[1,2,3] Ammar Jabali,[4,5,6] Delfina M. Romero,[1,2,3] Anne Houllier,[1,2,3] Florent Dingli,[7] Camille Maillard,[8,9] Anne Boland,[10] Jean-François Deleuze,[10] Damarys Loew,[7] Grazia M.S. Mancini,[11] Nadia Bahi-Buisson,[8,9,12,13] Julia Ladewig,[4,5,6] and Fiona Francis[1,2,3,14,*]

[1]INSERM U 1270, Paris, France
[2]Sorbonne University, UMR-S 1270, 75005 Paris, France
[3]Institut du Fer à Moulin, Paris, France
[4]Central Institute of Mental Health, Medical Faculty Mannheim, Heidelberg University, Mannheim, Germany
[5]HITBR Hector Institute for Translational Brain Research gGmbH, Mannheim, Germany
[6]German Cancer Research Center (DKFZ), Heidelberg, Germany
[7]Institut Curie, PSL Research University, Centre de Recherche, Laboratoire de Spectrométrie de Masse Protéomique, Paris, France
[8]Laboratory of Genetics and Development of the Cerebral Cortex, INSERM UMR1163 Imagine Institute, Paris, France
[9]Paris Descartes-Sorbonne Paris Cité University, Imagine Institute, Paris, France
[10]Centre National de Recherche en Génomique Humaine (CNRGH), Institut de Biologie François Jacob, CEA, Université Paris-Saclay, 91057 Evry, France
[11]Department of Clinical Genetics, Erasmus MC University Medical Center, 3015CN Rotterdam, the Netherlands
[12]Pediatric Neurology APHP-Necker Enfants Malades University Hospital, Paris, France
[13]Centre de Référence, Déficiences Intellectuelles de Causes Rares, APHP-Necker Enfants Malades University Hospital, Paris, France
[14]Lead Contact
*Correspondence: fiona.francis@inserm.fr
https://doi.org/10.1016/j.celrep.2019.06.096

SUMMARY

Apical radial glia (aRGs) are predominant progenitors during corticogenesis. Perturbing their function leads to cortical malformations, including subcortical heterotopia (SH), characterized by the presence of neurons below the cortex. *EML1/Eml1* mutations lead to SH in patients, as well as to heterotopic cortex (*HeCo*) mutant mice. In *HeCo* mice, some aRGs are abnormally positioned away from the ventricular zone (VZ). Thus, unraveling EML1/Eml1 function will clarify mechanisms maintaining aRGs in the VZ. We pinpoint an unknown EML1/Eml1 function in primary cilium formation. In *HeCo* aRGs, cilia are shorter, less numerous, and often found aberrantly oriented within vesicles. Patient fibroblasts and human cortical progenitors show similar defects. EML1 interacts with RPGRIP1L, a ciliary protein, and *RPGRIP1L* mutations were revealed in a heterotopia patient. We also identify Golgi apparatus abnormalities in *EML1/Eml1* mutant cells, potentially upstream of the cilia phenotype. We thus reveal primary cilia mechanisms impacting aRG dynamics in physiological and pathological conditions.

INTRODUCTION

The cerebral cortex is a highly organized structure whose development depends on different progenitor cell types. These give rise to post-mitotic neurons that migrate across the developing cortical wall to their final positions in the cortical plate. Apical radial glia (aRGs) are the main progenitor type in early corticogenesis and are responsible for the production of other progenitors, hence regulating the final neuronal output (Uzquiano et al., 2018). aRGs are localized in the proliferative ventricular zone (VZ) and have a characteristic morphology, including a basal process extending to the pial surface and an apical process descending to the ventricular surface. The apical process of aRGs terminates by an endfoot characterized by the presence of a centrosome that during interphase acts as a basal body docking a primary cilium. These two structures are crucial for aRG polarity and function, and abnormal behavior of aRGs disrupts neocortical development, causing severe cortical malformations (Bizzotto and Francis, 2015). Primary cilium anomalies, as well as defects in pathways dependent on this organelle, are expected to severely impact neural progenitor behavior as well as other steps of corticogenesis (Ding et al., 2019; Foerster et al., 2017; Gabriel et al., 2016; Wang et al., 2016; Guo et al., 2015; Higginbotham et al., 2013; Li et al., 2011; Wilson et al., 2012).

We and others identified pathogenic mutations in *EML1* in a specific group of cortical malformations characterized by atypical subcortical heterotopia (SH), corpus callosum agenesis, and macrocrania (Kielar et al., 2014; Shaheen et al., 2017). *EML1* codes for a microtubule-associated protein. Remarkably, a retrotransposon insertion disrupting the mouse ortholog *Eml1* leads to a similar phenotype in the heterotopic cortex (*HeCo*) mouse mutant (Croquelois et al., 2009; Kielar et al., 2014). The latter represents a unique model to decipher the biological basis of SH.

HeCo mice show progenitor anomalies from the early stages of corticogenesis thought to be responsible for the heterotopia phenotype (Bizzotto et al., 2017; Kielar et al., 2014). Some aRGs leave the VZ and divide in aberrant basal positions (Kielar et al., 2014). However, the pathological mechanisms leading to

This is an open access article under the CC BY-NC-ND license (http://creativecommons.org/licenses/by-nc-nd/4.0/).

the detachment of these cells in the *HeCo* VZ remain vastly unexplored.

The primary cilium is a microtubule-based antenna-like structure that serves as platform for signaling pathways. In aRG apical endfeet, this organelle protrudes within the ventricle in order to sense signals from the cerebrospinal fluid. It is formed after mitosis, when the centrosome, composed of two centrioles at the spindle pole, is trafficked toward the apical surface. During this journey, the centrosome associates with *de novo* synthesized membrane or ciliary remnants, which are often carried in vesicle-like structures and will then become the basal body-primary cilium complex (Bernabé-Rubio and Alonso, 2017; Paridaen et al., 2013). Once this complex reaches the plasma membrane, the basal body is docked and the primary cilium is inserted in the apical membrane. Trafficking of proteins from the Golgi apparatus is essential for the assembly of the basal body-primary cilium complex (Bernabé-Rubio and Alonso, 2017; Madhivanan and Aguilar, 2014). Therefore, correct formation of primary cilia depends on diverse subcellular processes that when disrupted could be responsible for the appearance of cilia-related pathologies (Madhivanan and Aguilar, 2014).

Here, we reveal a severe disruption of primary cilia in *Eml1*/*EML1* mutant conditions, not only in *HeCo* aRGs but also in patient fibroblasts and human induced pluripotent stem cell (iPSC)-derived cortical progenitors. Thus, Eml1/EML1 has an unexpected role in primary cilia formation. We also uncover a ciliary protein partner of EML1, RPGRIP1L, and report the first heterotopia patient showing mutations in this protein. Searching for upstream mechanisms potentially responsible for perturbed primary cilia, converging data pointed toward abnormal Golgi apparatus function in *Eml1*/*EML1* mutant conditions. We show here signs of abnormal Golgi structure and/or function in *HeCo* aRGs as well as patient fibroblasts and iPSC-derived cortical progenitors. We hence reveal perturbed Golgi apparatus mechanisms likely to be involved in primary cilium formation that most probably contribute to the aRG delamination phenotype.

RESULTS

Perturbation in Early Stages of Corticogenesis

Alterations in the number and distribution of γ-tubulin$^+$ and Arl13b$^+$ puncta, identifying centrosomes and primary cilia, respectively, were recently observed in the embryonic day 13.5 (E13.5) *HeCo* VZ (Bizzotto et al., 2017). For a view of the ventricular surface only, *en face* imaging was performed in combination with these two markers in wild-type (WT) and *HeCo* brains at the same developmental time point, together with immunostaining for F-actin, in order to delineate apical domains (Figure 1A). Using this approach, we confirmed a decrease of γ-tubulin$^+$ and Arl13b$^+$ puncta at the *HeCo* ventricular surface (Figures 1B and 1C). We further analyzed the total number of apical domains and quantified centrosome and primary-cilium-containing endfeet in WT and *HeCo* mice. All apical domains as well as centrosome-containing apical endfeet (with or without primary cilia) were decreased in the *HeCo* ventricular surface (Figures 1D–1F), in fitting with aRG delamination at E13.5 (Kielar et al., 2014). Apical domains not containing centrosome and primary cilia did not differ between *HeCo* and WT mice (Figure 1G).

Given that *Eml1* is expressed in the mouse VZ as early as E12.5 (Bizzotto et al., 2017), WT and *HeCo* cortices were also compared at this time point. First, a 30-min bromodeoxyuridine (BrdU) pulse was performed to analyze the position of cycling progenitor cells in the E12.5 cortical wall. Immunohistochemistry for BrdU and Ki67 confirmed the presence of a proportion of aberrant, superficially localized BrdU$^+$Ki67$^+$ progenitor cells as previously observed at E13.5 (Figures S1A and S1B; Kielar et al., 2014). At E12.5, *en face* imaging showed no significant change in the number of γ-tubulin$^+$ and Arl13b$^+$ puncta at the *HeCo* ventricular surface compared to WT, although tendencies for a decrease were observed, possibly indicating an incipient phenotype (Figures S1C–S1E). Apical domain and endfeet numbers were also analyzed, revealing tendencies similar to the E13.5 data (Figures S1F–S1I). A significant decrease in the number of centrosome and primary cilia containing apical endfeet per region of interest (ROI) was observed at E12.5 (Figure S1G). There was a slight but significant increase in the number of apical domains without centrosome and primary cilia at the *HeCo* ventricular surface (Figure 1I).

Analyses of the numbers of aRG endfeet at E12.5 and E13.5 support the hypothesis that some *Eml1* mutant aRGs delaminate from the ventricular surface at the early stages of corticogenesis.

Primary Cilia Formation Is Impaired in *Eml1* Mutant Conditions

We next questioned if, as well as reduced Arl13b puncta, primary cilia structure was abnormal in *HeCo* aRGs. Primary cilia length was first measured from *en face* Arl13b immunodetection, a parameter often studied to investigate defects in their assembly and/or disassembly (Kheradmand Kia et al., 2012). In addition to their decrease in number, primary cilia were found to be shorter at the *HeCo* ventricular surface at both E12.5 and E13.5 (Figures 1H, 1I, S1J, and S1K). Since the *HeCo* ventricular surface seemed more severely affected at E13.5, we focused on this stage to further understand the mechanisms involved.

In order to further examine the *HeCo* primary cilium phenotype, we analyzed their ultrastructure and subcellular localization in WT and *HeCo* brains at E13.5 by electron microscopy (EM) (Figure 2A). In WT aRG endfeet, centrioles are observed in close vicinity to the apical plasma membrane, the mother centriole acting as basal body and thus docking a primary cilium protruding in the ventricle (Figure 2A). In agreement with the *en face* imaging findings, aRG primary cilia measured from EM data were found to be shorter in *HeCo* compared to WT (Figures 2A–2C). In addition, when short cilia could be observed, these structures often lacked a properly formed basal body. Instead, densely packed microtubules were often present in place of centrioles (Figure 2A, white arrow). Furthermore, a significant increase in the number of cilia within vesicle-like structures was also evident in *HeCo* aRGs compared to WT (Figure 2A, black asterisk, and Figure 2D). These were often also mis-oriented basally rather than facing the ventricle (Figure 2A, white asterisk, and Figure 2E).

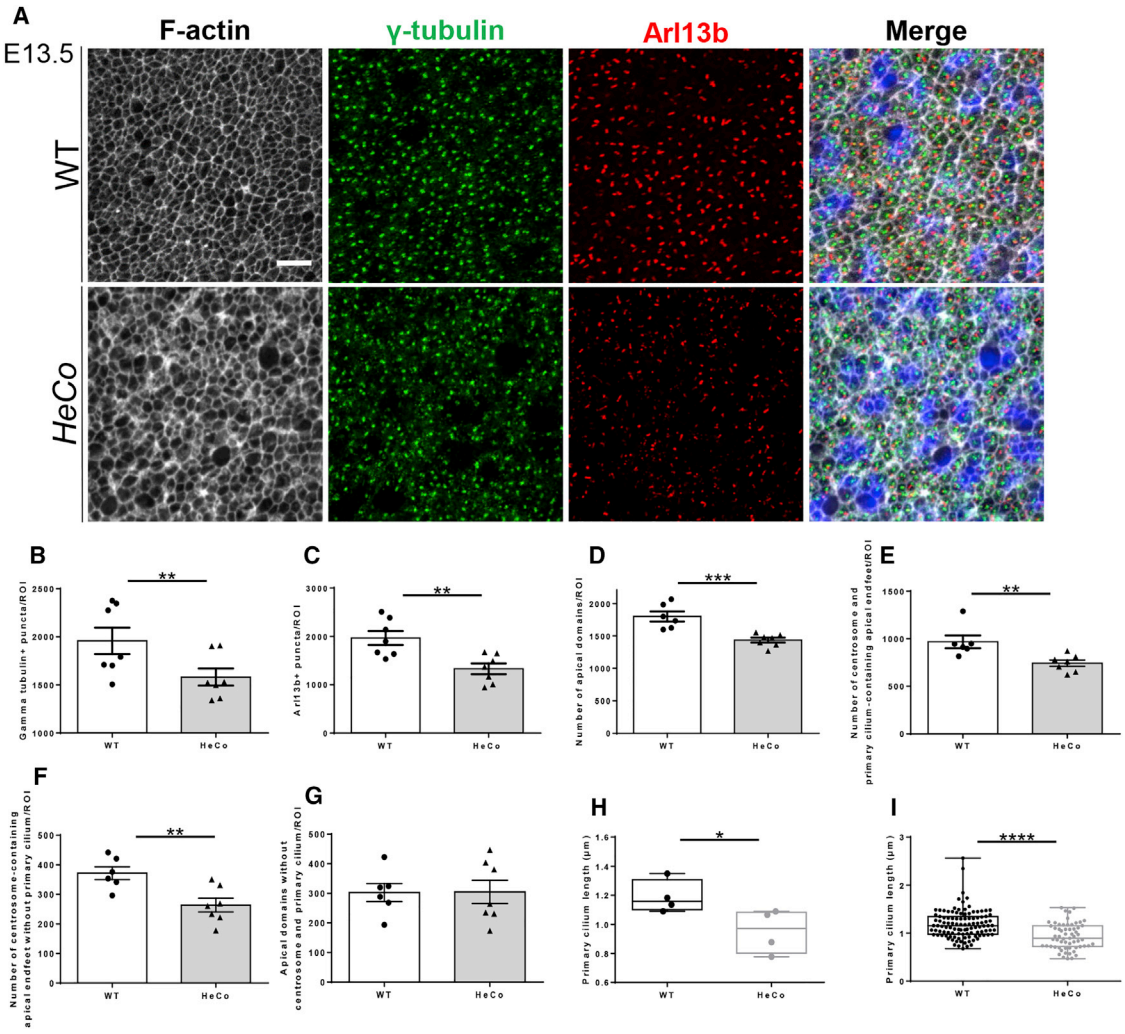

Figure 1. Centrosomes, Primary Cilia, and Apical Endfeet Are Decreased at the *HeCo* Ventricular Surface

(A) *En face* confocal imaging of the WT and *HeCo* ventricular surface using F-actin (white), anti-γ-tubulin (green), and anti-Arl13b (red) immunostaining.

(B) Quantification of γ-tubulin$^+$ puncta per ROI in WT and *HeCo* mice.

(C) Quantification of Arl13b$^+$ puncta per ROI in WT and *HeCo* mice.

(D) Quantification of number of apical domains in WT and *HeCo* mice.

(E) Quantification of centrosome and primary cilium-containing apical endfeet in WT and *HeCo* mice.

(F) Quantification of centrosome-containing apical endfeet without primary cilium in WT and *HeCo* mice.

(G) Quantification of apical domains without centrosome and primary cilium in WT and *HeCo* mice. This represents 17% and 20% of the total number of apical domains, respectively.

(H and I) Quantification of Arl13b$^+$ primary cilia length in WT (n = 5 from 3 litters, 110 primary cilia) and *HeCo* (n = 5 from 4 litters, 61 primary cilia). Each point represents an embryo (H) or primary cilium (I).

Each point in (B)–(G) represents an embryo (WT: n = 7 from 4 litters; *HeCo*: n = 6 from 5 litters). Scale bar, 10 μm (A). Data are represented as mean ± SEM and unpaired t test (B–G), and box and whisker plots show the median ± minimum-maximum range followed by Mann-Whitney test (H and I). ****$p < 0.0001$, ***$p < 0.0001$, **$p < 0.01$, and *$p < 0.05$.

See also Figure S1.

Thus, a decrease in the number and length of ventricular primary cilia, which are also often found within vesicles inside the cell, strongly suggests defects in their formation in *HeCo* aRGs during the early-to-middle (early-mid) stages of cortical development.

We also searched for potential primary cilia defects in other neuronal progenitor types. Upon Arl13b immunostaining, the E13.5 cortical wall of WT and *HeCo* mice was subdivided in six equally sized bins. An increased proportion of Arl13b puncta was identified in upper-VZ/subventricular zone (SVZ)-containing bin 4 (with a decrease in the SVZ/intermediate zone [IZ]-containing bin 5) in *HeCo* cortices (Figures S1L and S1M). These preliminary data may indicate that primary cilia are also abnormal in other progenitors populating more basal regions of the developing cortex.

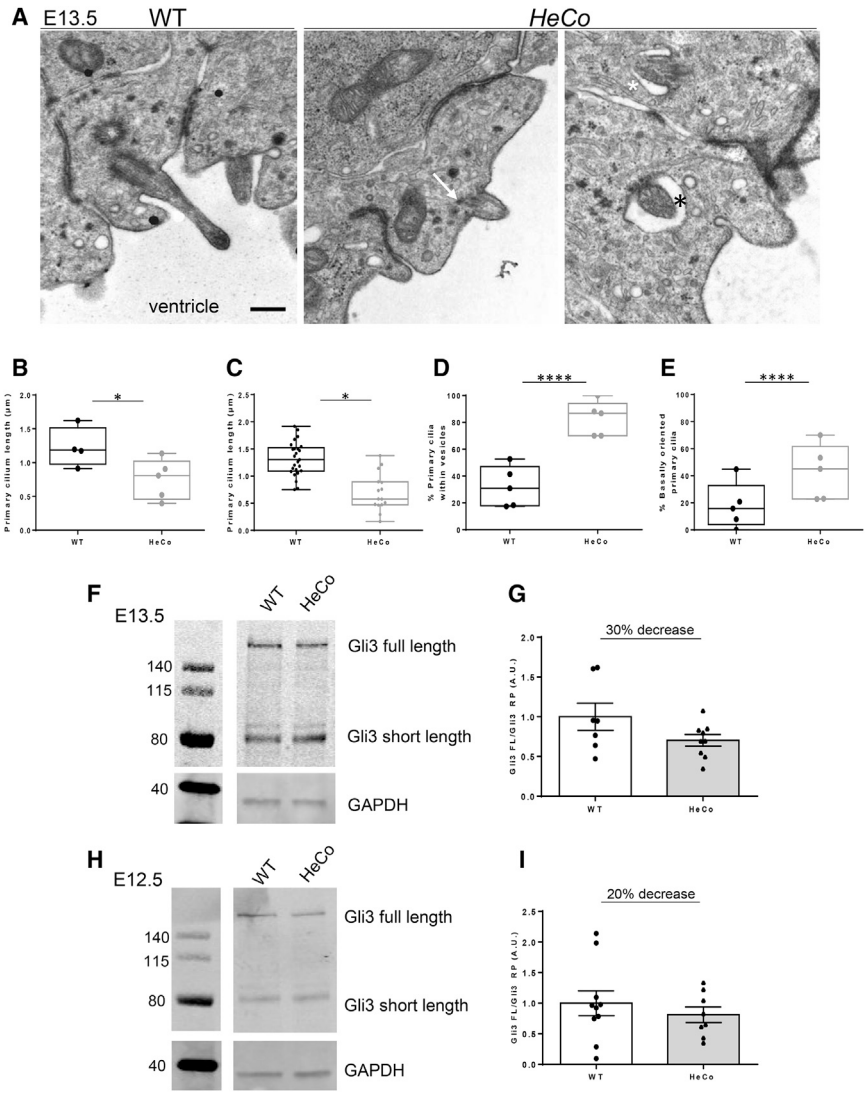

Figure 2. Primary Cilia Formation Is Impaired in *Eml1* Mutant Conditions, although No Changes in Shh Signaling Were Observed

(A) Representative images of EM acquisitions of the apical surface of WT and *HeCo* brains. White arrow shows that the basal body is not properly assembled in *HeCo* aRGs. Instead, densely packed microtubules are observed. The black asterisk indicates apically oriented primary cilium within a vesicle. The white asterisk indicates basally oriented primary cilium within a vesicle.

(B and C) Quantification of primary cilium length in WT (n = 4 embryos from 3 litters, 25 primary cilia) and *HeCo* (n = 5 embryos from 3 litters, 15 primary cilia) VZ. Each point represents an embryo (B) or a primary cilium (C).

(D and E) Percentage of primary cilia found within vesicles in WT and *HeCo* VZ (D), and percentage of basally oriented primary cilia in WT and *HeCo* VZ (E). Each point represents an embryo (n = 5 per condition from 3 litters; 150–169 cells). Statistical tests were performed considering the frequency across cells analyzed.

(F) Representative western blot of WT and *HeCo* E13.5 cortical lysates immunodetected for Gli3 and GAPDH.

(G) Quantifications from E13.5 western blots, with band intensities normalized to GAPDH (WT: n = 9 embryos from 2 litters; *HeCo*: n = 7 embryos from 2 litters).

(H) Representative western blot of WT and *HeCo* E12.5 cortical lysates immunodetected for Gli3 and GAPDH.

(I) Quantifications from E12.5 western blots, with band intensities normalized to GAPDH (WT: n = 10 embryos from 2 litters; *HeCo*: n = 8 embryos from 2 litters).

Scale bar, 0.5 μm (A). Box and whisker plots show the median ± minimum-maximum range followed by Mann-Whitney test (B and C) or chi-square test (D and E) or mean ± SEM (G and I). ****$p < 0.0001$ and *$p < 0.05$.

There Are No Major Changes in *HeCo* Cortex Shh Signaling at Early-Mid Corticogenesis

Primary cilia are central for the transduction of Sonic hedgehog (Shh) signaling (Wheway et al., 2018). Conditional knockout mice of ciliary proteins often show changes in Shh signaling in the developing brain impacting the levels and/or processing of its downstream effectors, notably the Gli transcription factors (Besse et al., 2011; Willaredt et al., 2008; Wilson et al., 2012). Gli proteins are found in a short-length (SL) repressor form or in a full-length (FL) activator form upon Shh stimulation. The primary cilium phenotype observed in *HeCo* aRGs prompted us to analyze this pathway. We analyzed the levels of Gli3 in cortical lysates from *HeCo* and WT mice at E12.5 and E13.5 by western blot (Figures 2F–2I). There was a tendency toward a decreased Gli3 full-length:Gli3 short-length ratio in *HeCo* cortices (Figures 2G and 2I) that was stronger at E13.5 than E12.5, the stage at which the severest primary cilia phenotype was observed. Despite these consistent subtle differences, there were no significant Shh changes observed between *HeCo* and WT E12.5/E13.5 cortical lysates.

Protein Partners of Eml1 Help Indicate that *RPGRIP1L* Is a Heterotopia Gene

Eml1 appears to have crucial functions regulating aRG behavior (Kielar et al., 2014; Bizzotto et al., 2017; this study), although the molecular pathways in which it is involved have not yet been clearly linked to aRG phenotypes. Performing a comprehensive analysis of potential Eml1-interacting partners identified in a previous screen (Bizzotto et al., 2017), the ciliary protein Rpgrip1l was identified. This protein is known to localize to the base of the primary cilium, in the transition zone, and mutations were previously identified in Joubert and Meckel ciliopathy syndromes (Wiegering et al., 2018). To confirm the interaction between Eml1 and Rpgrip1l, Neuro2A cells were co-transfected with FLAG-tagged EML1 and c-*myc*-tagged RPGRIP1L plasmids. 48 h later, antibodies directed at the tag of one of the proteins

(e.g., anti-FLAG; Figure 3A) were incubated with cell lysates to capture the protein of interest. Protein G Sepharose was added to capture the antibody-protein complexes, and after elution, these were then separated on protein gels. Immunodetection of western blots was performed with antibodies directed against the opposing protein tag (e.g., anti c-*myc*). Co-immunoprecipitation (coIP) experiments were performed in both directions, and this confirmed the interaction between EML1 and RPGRIP1L with either anti-FLAG (Figure 3A) or anti-c-myc (Figure 3F) antibodies used for the initial precipitation. These results further support that EML1 may play a role in primary-cilium-related protein complexes.

Simultaneously, compound heterozygous variations in *RPGRIP1L* (GenBank: NM_015272.2) were identified in a patient (P700-5) with SH (Figures 3B–3D; Table S1). P700-5 also exhibited agenesis of the corpus callosum and cerebellar dysplasia (Figures 3D4 and 3D5; Table S2). Nucleotide variations in *RPGRIP1L* were confirmed by Sanger sequencing. A c.3706C>T pathogenic variation in exon 24 (R1236C, sorting intolerant from tolerant [SIFT; https://sift.bii.a-star.edu.sg/] 0.03, damaging) was transmitted from the father. A c.3562G>A nucleotide change in exon 22 (V1188M, SIFT tolerated) was transmitted from the mother (Figure 3C; Table S1). Since autosomal recessive mutations in *RPGRIP1L* have previously been associated with Joubert and Meckel syndromes (OMIM: 610937), the unusual C-terminal mutations identified here (Figure 3E) may be important for the cortical phenotype observed.

Given the interaction of EML1 and RPGRIP1L and the resemblance of the phenotypes found in patients, we postulated that the interaction between these proteins may be altered in the presence of patient mutations. Both individual RPGRIP1L mutations led to a dramatic loss of interaction with EML1, using either anti-FLAG or anti-c-*myc* (Figures 3F, 3G, S2A, and S2B) for immunoprecipitation. The RPGRIP1L interaction was also tested using an EML1 construct expressing a patient mutation (family P135, mutation T243A; Kielar et al., 2014). Under these conditions, dramatically reduced quantities of FLAG-EML1-T243A were observed in anti-c-myc immunoprecipitates (Figure 3G). These data confirm that when either RPGRIP1L or EML1 is mutated, the interaction between the proteins is compromised.

These combined data suggest that convergent primary-cilia-related mechanisms are responsible for the heterotopia in *EML1* and *RPGRIP1L* patients. We then assessed the localization of RPGRIP1L mutant proteins in a human cell line (retinal pigmented epithelial cells [RPE1 cells]). RPE1 cells were transfected with recombinant c-*myc*-RPGRIP1L WT, c-*myc*-RPGRIP1L-R1236C, or c-*myc*-RPGRIP1L-V1188M. While WT RPGRIP1L clustered in perinuclear regions with a puncta-like pattern (white box), as previously shown for this protein (Gerhardt et al., 2015), the same type of staining was not observed when transfecting cells with the mutant constructs (Figure S2C). This suggests an altered subcellular localization of RPGRIP1L expressing heterotopia mutations.

To begin to test the impact of the individual *RPGRIP1L* heterotopia mutations at the early stages of corticogenesis, they were overexpressed in WT mouse brain. *In utero* electroporation at E13 was performed of individual c-*myc*-RPGRIP1L mutant constructs with a pCAG-IRES-GFP (pCAGIG) reporter construct to identify electroporated cells, as well as an Arl13b-RFP construct targeting the primary cilium. At E14, $Pax6^{+}GFP^{+}$ cells were quantified across six equally sized bins spanning the cortical wall, and the percentage of cells in the region encompassing the VZ was assessed (bins 1–3) compared to the SVZ, IZ, and cortical plate [CP; bins 4–6; Figure S2D). Mutant forms of RPGRIP1L, especially the V1188M mutation, led to an apparent shift of $Pax6^{+}GFP^{+}$ and $Pax6^{+}GFP^{-}$ cells to basal positions in the cortical wall (Figure S2E). In addition, the c-*myc*-RPGRIP1L V1188M construct showed the presence of polarized rosette-like structures composed of primary cilia-containing $Pax6^{+}$ cells in abnormal superficial regions (two out of three embryos; Figure S2F). Internalization of $Pax6^{+}$ cells has previously been associated with primary cilia defects (Higginbotham et al., 2013; Lien et al., 2006).

Primary Cilia Formation Is Impaired in *EML1* and *RPGRIP1L* Patient Fibroblasts

Convergent suggestions for a link between primary cilia and heterotopia led us to assess the growth dynamics of this organelle in human patient fibroblasts. A cell culture approach for analyzing primary cilia assembly and/or disassembly was adopted (Kheradmand Kia et al., 2012). Five different lines of human fibroblasts were cultured from two *EML1*-patients (P3489 and P135; Kielar et al., 2014), the above-described *RPGRIP1L*-heterotopia patient (P700), and two similarly aged controls (control 1 and control 2). We studied primary cilium formation (1) under basal conditions (72 h after plating), when cells are asynchronously dividing; and (2) after serum starvation (SS), which was performed for 48 or 96 h (Figures 4A–4E, S3A, and S3B). SS induces cells to enter quiescence (G0) and thus grow a primary cilium (Figure S3A).

The percentage of cells presenting a primary cilium in the three different conditions was analyzed. Under basal conditions (Figure 4B) and 48 h after SS (Figure S3C), each of the three patient lines showed significantly fewer cells possessing a primary cilium. At 96 h, one of the EML1 patient lines (P3489) reached levels similar to those of the control lines, while the other patient lines continued to show a significantly decreased proportion of primary-cilium-containing fibroblasts (Figure 4D). Under basal conditions and 48 h after SS, primary cilia length did not seem to be severely compromised compared to control lines (although the P135 and P700 fibroblast lines showed a tendency to have shorter primary cilia; Figures 4C and S3D). However, when performing SS for 96 h, all patient lines showed a significant decrease in the length of primary cilia compared to control conditions (Figure 4E).

These results suggest that *EML1*- and *RPGRIP1L*-mutant cells do not assemble cilia efficiently, in fitting with a role for EML1 and RPGRIP1L in primary cilium formation. Importantly, *RPGRIP1L* patient fibroblasts showed the same dynamics as *EML1* patient fibroblasts, further suggesting that perturbed mechanisms underlying the heterotopia phenotype may converge.

Human Cortical Progenitors with *EML1* Mutations Also Show Primary Cilia Anomalies

We decided to further analyze primary cilia in human cortical progenitor cells *in vitro*. These were differentiated from

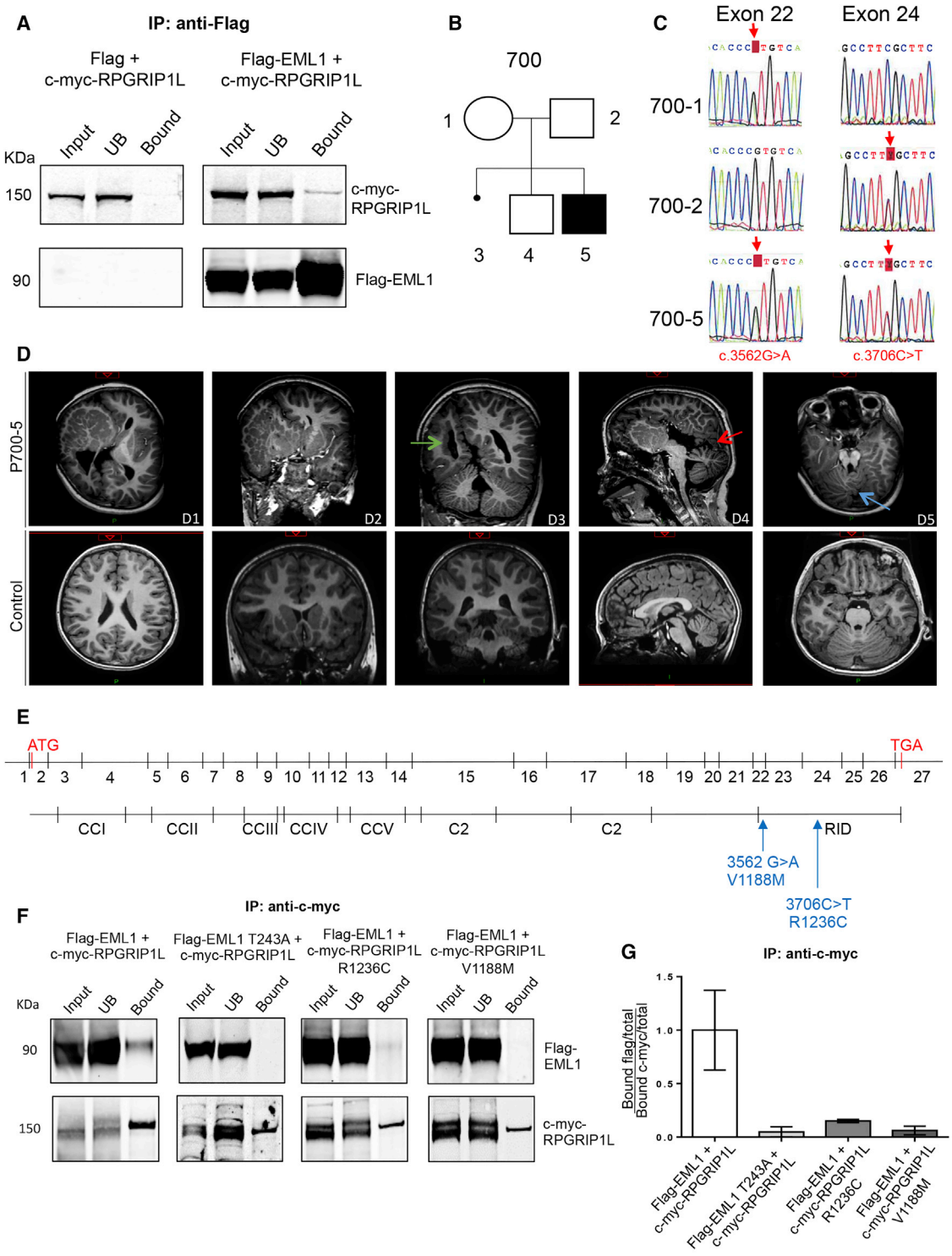

Figure 3. EML1 Interacts with RPGRIP1L, in which Mutations Were Identified in a Heterotopia Patient

(A) Representative western blots showing immunoprecipitation with anti-FLAG when co-transfecting FLAG/FLAG-EML1 with c-*myc*-RPGRIP1L (3 experiments per condition). The FLAG peptide alone (1 kDa) is a short sequence not recognized under these western blot conditions. Input: cell lysate prior to IP; UB (unbound) corresponds to the fraction of proteins not attaching to the bait (here FLAG-tagged protein).

(B) Pedigree of the family (P700), with one healthy boy, one affected boy, and one miscarriage.

(C) Sanger sequence chromatograms for the parents and affected child of a portion of the *RPGRIP1L* gene. Compound heterozygous mutations were identified in patient 700-5 (red arrows), one inherited from the mother and one from the father. Nucleotides are shown in red (T), black (G), green (A), and blue (C).

(legend continued on next page)

iPSCs from two control individuals and two *EML1*-mutation patients (controls 1.1 and 2.1, P3489, and P135; Figure S3E; Kielar et al., 2014; Gaspard et al., 2008; Shi et al., 2012). EM analyses of control-line-derived cortical cultures revealed the presence of a mother centriole docking a properly arranged primary cilium surrounded by ciliary pockets (Figure 4F). When investigating primary cilia in patient-derived cortical progenitors, we had difficulty identifying these organelles and those primary cilia observed showed abnormalities, including disturbed ciliary-like structures with no proper microtubule arrangement (Figure 4F, P135) or ciliary pockets that appeared distended (Figure 4F, P3489). Thus, the primary cilium also appears perturbed in human patient-derived cortical progenitors, suggesting a conserved role of Eml1/EML1 across evolution.

Subcellular Localization and EML1-Interacting Proteins Shed Light on Potential Pathways Involved in the Centrosome-Primary Cilia Phenotype

EML1 has a cell-cycle-dependent localization in mouse neuronal progenitor cells *in vitro* (Kielar et al., 2014). It co-localizes with the microtubule network in interphase Vero cells (Kielar et al., 2014); however, a ciliary localization has not been described for this protein family (Fry et al., 2016). Its localization was hence further explored in aRGs, as well as in ciliated RPE1 cells, using exogenous expression of an EML1-tagged plasmid, since there are no known reliable antibodies to detect the endogenous protein. Transfection of YFP-EML1 in RPE1 cells showed recombinant EML1 throughout the cytoplasm, including in perinuclear regions, with no obvious association with the primary cilium (Figure S4A). *In utero* electroporation of pCAG-IRES-Tomato (to delineate aRG morphology) and EGFP-EML1 identified recombinant EML1 ubiquitously expressed in aRG apical processes (Figure S4B).

To learn more about EML1's cellular role, we screened for additional interacting partners using full-length EML1, differing from the previous screen, which used only the N terminus (Bizzotto et al., 2017). Indeed, most mutations fall in the C-terminal β propeller structure (Fry et al., 2016), indicating the potential importance of this domain. Pull-down experiments were performed with purified Strep-tagged full-length EML1 and E13.5 WT mouse cortex lysates (Figure 5A). Captured proteins were identified by mass spectrometry (MS). Label-free quantitative analyses based on the extracted ion chromatogram (XIC) method revealed a list of 240 proteins enriched in the Strep-tagged EML1 condition (Table S3). We compared this 240-protein list with the N-terminal interactors identified previously (Bizzotto et al., 2017). 85 out of 240 proteins commonly interacted with both the EML1 N-terminus and the full-length protein, confirming the specificity of the new screen (Figure 5 B). The remaining proteins may be specific for interactions with the EML1 C-terminal domain.

To further identify cytoplasmic proteins, the new 240-protein list was further filtered to exclude nuclear proteins (as previously performed in Bizzotto et al., 2017), and a final list of 113 proteins was obtained (Table S3). The expression pattern across the murine developing cortex (E14.5) was examined for genes encoding these proteins using publicly available resources (GenePaint [https://gp3.mpg.de/]; data were available for 71 out of 113 proteins; Figure 5C). 63.4% of the 113 proteins clearly showed expression in the VZ (8.9% showed a CP expression only, and a further 27.7% were of unknown expression).

Cilia-related proteins were identified in both N-terminal and full-length lists (Table S4), revealing a total of 42 potential cilia-related EML1 interactors. Gene Ontology (GO) analyses for the 113-protein list were performed using the DAVID (Database for Annotation, Visualization and Integrated Discovery functional annotation tool [https://david.ncifcrf.gov/home.jsp]) and STRING (Search Tool for the Retrieval of Interacting Genes/Proteins [https://string-db.org]) publicly available resources (Figure 5D; Tables S4, S5, and S6). Cell-cell adhesion, microtubule and actin-associated proteins, and Golgi-derived protein transport were identified among other categories in DAVID GO analyses (Figure 5D; Tables S4 and S5). STRING analyses revealed similar results, including membrane-bounded organelle, cytoskeleton, and cell junction among the most enriched "cellular component" GO categories (Table S6). Thus, in addition to cilia proteins, several other categories of proteins point to previously uncharacterized roles for EML1.

Golgi-Related Protein Partners of EML1, Including VCIP135

The prominent apical process localization of recombinant EML1 in interphase aRGs, as well as the GO categories identified, prompted us to further focus on protein trafficking from the Golgi apparatus, localized in aRG apical processes (Taverna et al., 2016).

Given the importance of cargo trafficking and Golgi-derived protein transport for primary cilium formation, we searched for Golgi-related proteins in the MS lists (Table S4). VCIP135 (also known as VCPIP1) showed high specificity for the EML1-bound condition. This protein mediates Golgi apparatus cisternae regrowth after mitosis as well as maintenance of this organelle during interphase. Knockdown of VCIP135 is known

(D) Representative T1-weighted section of brain magnetic resonance imaging (MRI) of P700-5 and control showing a unilateral, extensive, subcortical heterotopia spanning from the frontal lobe (D1) to the parieto-temporal region (D2). In the occipital lobe, the cortical malformation is characterized by right-sided nodular periventricular subependymal heterotopia (D3, green arrow). Note that the overlying cortex is thinner and appears dysplastic (D1–D3). P700-5 presents corpus callosum agenesis (D4, red arrow) and cerebellar dysplasia (D5, blue arrow).

(E) Schematic representation of the *RPGRIP1L* gene (above) and protein domains (below). Blue arrows indicate the position of compound heterozygous mutations found in P700-5.

(F) Representative western blot of immunoprecipitation with anti-c-*myc* when co-transfecting (WT or mutant) FLAG-EML1 with (WT or mutant) c-*myc*-RPGRIP1L (3 experiments per condition).

(G) Quantification of immunoprecipitation experiments comparing the amount of EML1 bound to RPGRIP1L in WT and mutant conditions. The bound prey protein was normalized to total levels of the protein and immunoprecipitated bait protein. Data are represented as mean ± SEM.

See also Figure S2.

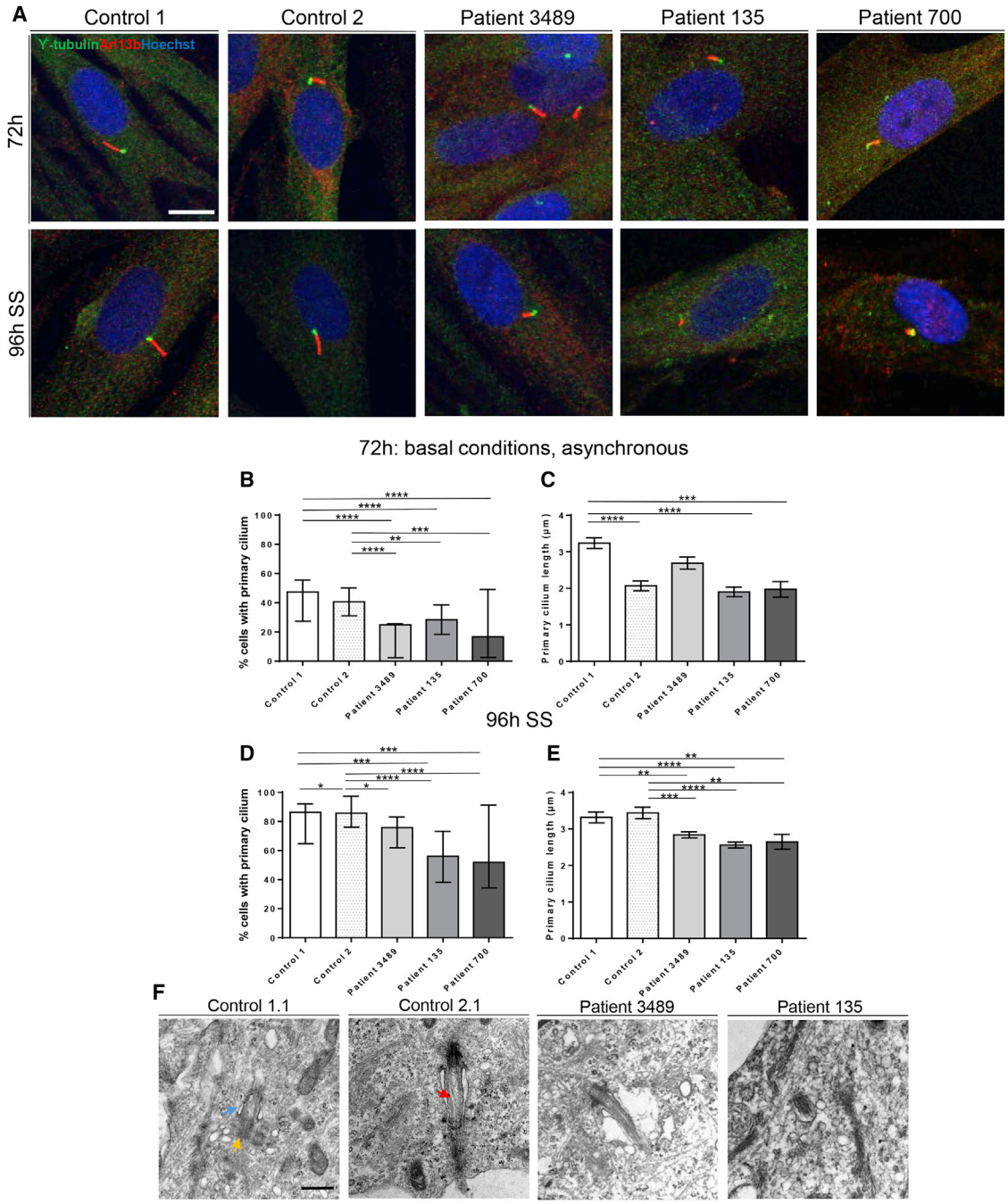

Figure 4. Primary Cilium Formation Is Perturbed in *EML1* and *RPGRIP1L* Patient Fibroblasts and Cortical Progenitors Differentiated from *EML1* Patient-Derived iPSCs

(A) Representative images of immunocytochemistry for γ-tubulin (green) and Arl13b (red) in control (control 1 and 2) and patient fibroblasts (P3489: EML1 W225R; P135: EML1 T243A R138X; and P700: RPGRIP1L R1236C V1188M) at basal conditions (72 h) and 96 h after serum starvation (SS).

(B) Percentage of fibroblasts presenting a primary cilium in basal conditions (2–4 experiments per condition).

(C) Quantifications of primary cilium length in fibroblasts in basal conditions (n = 24–109 primary cilia from 2 to 4 experiments).

(D) Percentage of fibroblasts presenting a primary cilium at 96 h SS (3–4 experiments per condition).

(E) Quantifications of primary cilium length in fibroblasts at 96 h SS. n = 64–141 primary cilia from 3 to 4 experiments.

(F) Representative EM images of human cortical progenitors derived from control and *EML1* mutation patient iPSCs. Yellow arrow, basal body; blue arrow, ciliary pockets; and red arrow, primary cilium.

Scale bars, 10 μm (A) and 0.5 μm (F). Data are represented as median ± minimum-maximum range and chi-square test (B and D) or mean ± SEM and one-way ANOVA followed by unpaired t test (C and E). ****$p < 0.0001$, ***$p < 0.001$, **$p < 0.01$, and *$p < 0.05$.

See also Figure S3.

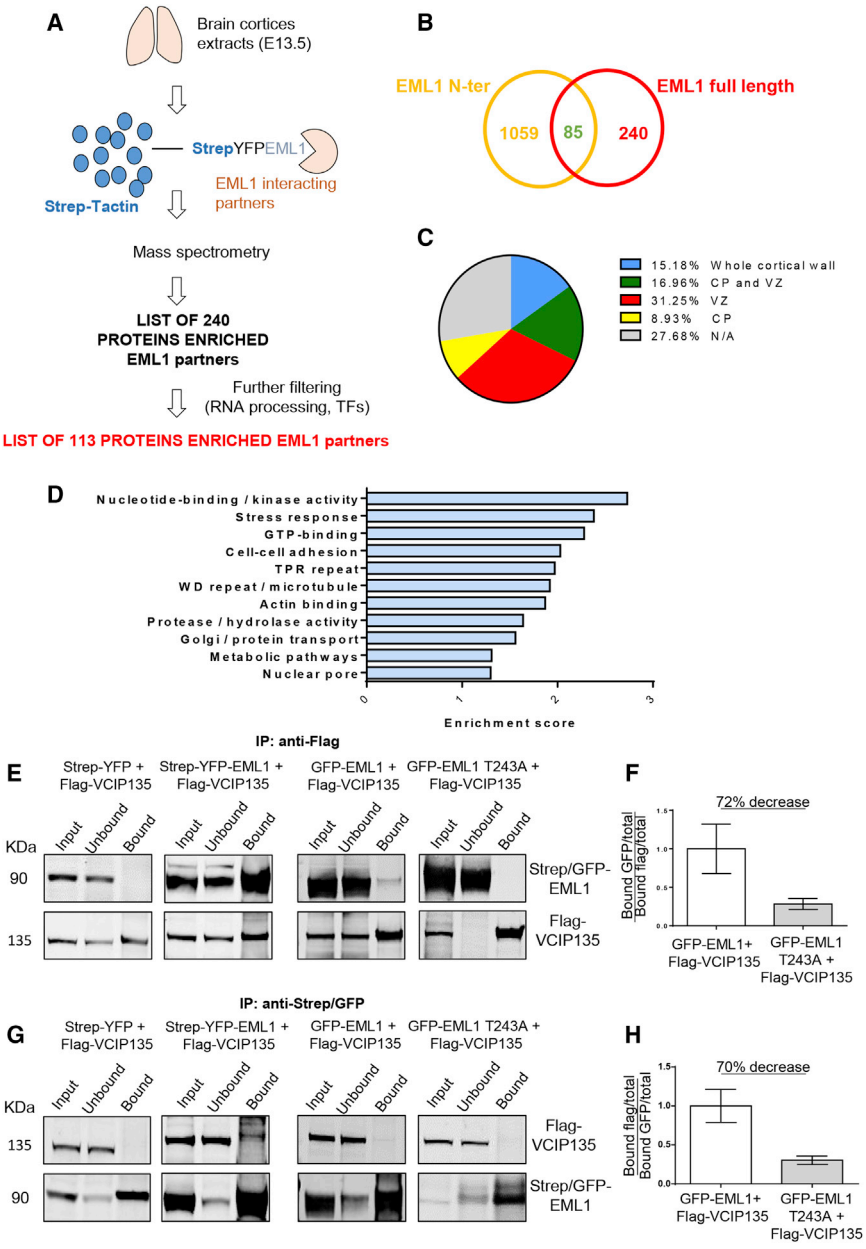

Figure 5. Mass Spectrometry Analyses Reveal Additional EML1-Interacting Partners, among Them the Golgi Protein VCIP135

(A) Schematic of the proteomics workflow. Either Strep-YFP or Strep-YFP-EML1 purified with Strep-Tactin beads was used for pull-down experiments using embryonic cortex lysates. Binding partners were obtained by quantitative label-free MS analyses performed from four replicates.

(B) Diagram indicating number of common proteins identified in full-length and N-terminal (Bizzotto et al., 2017) EML1 MS screens.

(C) Diagram representing expression of EML1-interacting partners in the E14.5 murine cortical wall (GenePaint).

(D) Gene Ontology analyses performed with the publicly available software DAVID for the 113-protein list. Only those categories with an enrichment score >1 are represented.

(E) Representative western blot of immunoprecipitation with anti-FLAG when co-transfecting FLAG-VCIP135 with Strep-YFP, Strep-YFP-EML1, GFP-EML1, and GFP-EML1-T243A (2–3 experiments per condition).

(F) Quantification of immunoprecipitation experiments comparing the amount of EML1 bound to VCIP135 in WT and mutant conditions. The bound prey protein was normalized to total levels of the protein and levels of the bait protein.

(G) Representative western blot of immunoprecipitation with Strep or GFP when co-transfecting Strep-YFP with FLAG-VCIP135, Strep-YFP-EML1 with FLAG-VCIP135, GFP-EML1 with FLAG-VCIP135, and GFP-EML1-T243A with FLAG-VCIP135 (2–3 experiments per condition).

(H) Quantification of immunoprecipitation experiments comparing the amount of VCIP135 bound to EML1 in WT and mutant conditions. The bound prey protein was normalized to total levels of the protein and levels of the bait protein.

Data are represented as mean ± SEM (F and H). See also Figures S4 and S5.

to lead to Golgi fragmentation (Uchiyama et al., 2002; Zhang et al., 2014; Zhang and Wang, 2015). The interaction of Strep-tagged EML1 with FLAG-tagged VCIP135 was tested by performing coIP experiments in Neuro2A cells. An interaction was confirmed using either anti-FLAG or Strep for the IP (Figures 5E and 5G). We next checked if EML1 mutation perturbed this interaction, performing coIP experiments with GFP-EML1 T243A and FLAG-VCIP135. Using anti-FLAG and anti-GFP, a reduction of the interaction between the two proteins was observed (Figures 5E–5H). Therefore, a patient mutation in the β propeller domain of EML1 disrupts the interaction with VCIP135, suggesting that EML1 may play a role associated with the Golgi apparatus.

We next decided to knock down (KD) *Vcip135* in aRGs at E13 (Figure S5A), a time when ectopic aRGs are found in *Eml1* mutant conditions (Kielar et al., 2014). A miRNA-embedded short hairpin (shmiRNA) against *Vcip135* and a scrambled control shmiRNA (shmiRNA control) were generated. Efficiency was tested (reduction by 40 %) by performing transfections of these constructs in Neuro2A cells, followed by qRT-PCR (Figure S5B). *In utero* electroporation together with a pCAG-IRES-Tomato construct was performed at E13, and brains were analyzed 24 h later (Figure S5A). Tomato$^+$ cells were quantified across six equally sized cortical bins. A significant shift of Tomato$^+$ cells was observed from bins 1 to 3 toward more basal positions in the *Vcip135* KD condition (Figure S5C). This suggests that Golgi-related proteins, and more specifically the Eml1-interacting protein Vcip135, are important for progenitor cell position.

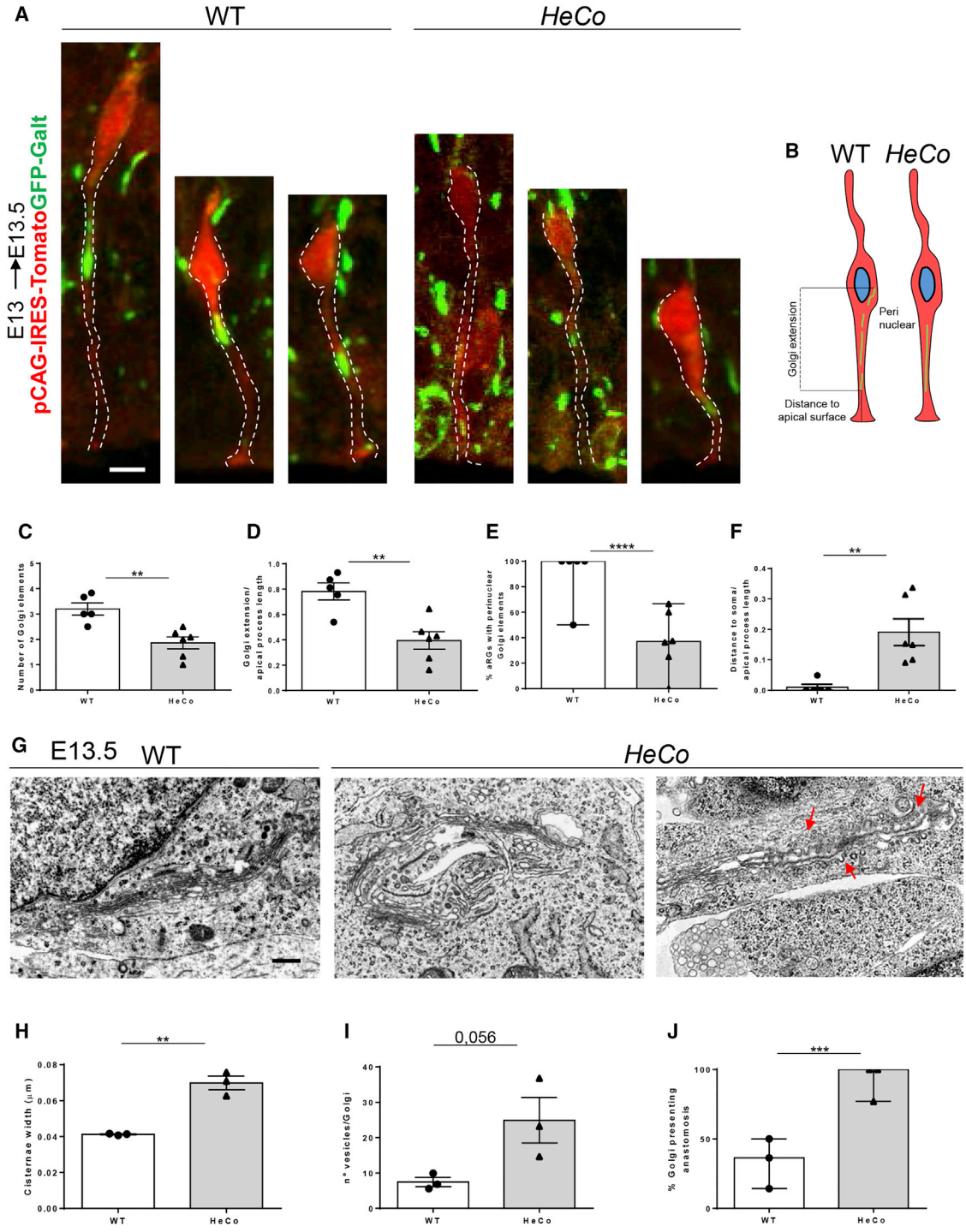

Figure 6. The Golgi Apparatus Is Severely Disrupted in *Eml1* Mutant aRGs in Brain Slices

(A) WT and *HeCo* aRGs electroporated with pCAG-IRES-Tomato (cell morphology) and pCAG-Galt-EGFP (Golgi apparatus).

(B) Schema representing the parameters quantified and the Golgi phenotype observed in aRGs.

(C) Quantification of number of Golgi elements.

(D) Quantification of Golgi extension.

(E) Quantification of the percentage of cells containing perinuclear Golgi elements. Statistical tests were performed considering the frequency across cells analyzed.

(F) Quantification of the distance between the basal-most Golgi element to the aRG soma.

(G) Representative EM images of the Golgi apparatus in WT and *HeCo* aRGs at E13.5. Red arrow shows anastomosis.

(legend continued on next page)

The Golgi Apparatus Is Severely Disrupted in *HeCo* Neuronal Progenitors

A Golgi localization for recombinant Eml1 could not be easily identified in Pax6$^+$ neuronal progenitors due to the abundant soluble fraction of the protein (Figure S4C). We decided to query this organelle in *HeCo* aRGs. The Golgi apparatus has recently been described to be restricted to aRG apical processes, where it exists as a series of individualized stacks (Taverna et al., 2016), defined here as ''Golgi elements.'' *In utero* electroporation of a pCAG-IRES-Tomato plasmid, as well as a pCAG-Galt-EGFP plasmid targeting the Golgi apparatus, was performed at E13, and WT and *HeCo* brains were analyzed at E13.5. Golgi position was assessed in WT and *HeCo* aRGs as in Taverna et al. (2016), and the number of perinuclear Golgi elements was also assessed.

Golgi apparatus distribution was strikingly different in *HeCo* compared to WT aRGs at E13.5 (Figures 6A–6F). The number of Golgi elements was significantly reduced, as was the extension of this organelle in the apical process (Figures 6C and 6D). Consistently, there were fewer Golgi elements in perinuclear regions, and these were further away from the soma (Figures 6E and 6F). These data indicate that in the *HeCo* VZ the Golgi apparatus is subdivided in fewer stacks and does not span as far across the apical process of aRGs (depicted in Figure 6B).

In order to further examine the Golgi apparatus phenotype, several parameters were assessed by EM (Figures 6G–6J). Golgi cisternae width was significantly increased in *HeCo* aRGs (Figures 6G and 6H), and there was a tendency for increased vesicles surrounding this organelle (Figure 6I). We also assessed if the Golgi apparatus showed signs of anastomosis, a process characterized by the fusion and aberrant branching of Golgi cisternae. Indeed, there was a significant increase in the anastomosis-presenting Golgi apparatus in *HeCo* compared to WT aRGs (Figure 6G, red arrows, and Figure 6J). These abnormal Golgi features point toward a pathological disruption of this organelle.

The multiple Golgi apparatus phenotypes suggest there may also be functional Golgi alterations in *HeCo* aRGs. An *in vitro* approach was established to assess Golgi-derived trafficking in aRG-like cells in culture. Pax6$^+$ progenitor-enriched cell cultures (Sun et al., 2011) were prepared from the dorsal telencephalon of E13.5 WT and *HeCo* embryos (Figure 7A). These cells were transfected with the thermosensitive vesicular stomatitis virus G protein VSVts405-G-EGFP (VSVG-EGFP). This modified protein is stored in the endoplasmic reticulum (ER)-Golgi compartments when cells are incubated at 39.5°C. Upon incubation at 32°C, the protein starts to exit these compartments and is trafficked toward the plasma membrane (Alterio et al., 2015; Bergmann, 1989). Using this approach combined with immunocytochemistry for the Golgi marker GM130, VSVG-EGFP anterograde trafficking was analyzed 5 and 30 min after incubation at 32°C (Figure 7B). The presence or absence of GFP$^+$ puncta outside the Golgi apparatus was assessed at these two time points, and the number of puncta was quantified. As expected, 5 min after incubation at 32°C, most of the VSVG-EGFP protein was found within the Golgi both in WT and *HeCo* cells, with only some sparse GFP$^+$ puncta found in the cytoplasm (average of two puncta per cell in both conditions; data not shown; Figures 7B and 7C). However, analyses at 30 min showed fewer *HeCo* cells presenting GFP$^+$ puncta outside of the Golgi (17% decrease) (Figures 7B and 7D). This decrease was significant when considering 2 GFP$^+$ puncta/cell as the baseline (Figure 7E). *HeCo* cells also showed a lower overall number of GFP+ puncta compared to WT cells (Figure 7F). Our data hence converge to suggest that Golgi apparatus structure and its anterograde transport are perturbed in *HeCo* cells, with a reduction in post-Golgi trafficking demonstrated in the VSVG-EGFP assay.

EML1 Patient Fibroblasts and Human Cortical Progenitors Also Show Golgi Anomalies

We queried if the Golgi apparatus was also perturbed in *EML1* patient fibroblasts. The Golgi marker TGN46 was assessed in basal conditions (72 h), quantifying the number of Golgi fragments as well as Golgi volume (Figures S5D–S5F). P135 patient cells showed an increased number of Golgi fragments as well as an increased volume, and the P3489 line showed similar tendencies (Figures S5D–S5F).

We also assessed the Golgi apparatus by EM in human cortical progenitors derived from either control or EML1 patient iPSCs (Figure 7G). Control line-derived cortical progenitors exhibited a flat cisternae-containing Golgi apparatus. This was, however, not true for the EML1 patient samples. Here, we observed a significant increase in the percentage of cells presenting vacuolized Golgi (Figure 7G, red asterisk, and Figure 7H). Primary cilia defects were previously found to be associated with anomalies of Golgi-dependent processes (Hua and Ferland, 2018). EML1 mutant Golgi apparatus defects are hence likely to be associated with the severe primary cilium defects identified.

DISCUSSION

Our study unravels an unprecedented role for Eml1/EML1 in primary cilia formation. Through a plethora of approaches, we report severe anomalies in this organelle in Eml1/EML1 mutant conditions and confirm an EML1 ciliary protein partner, RPGRIP1L. We identified a first heterotopia patient presenting

(H) Quantification of cisternae width.
(I) Quantification of the number of vesicles surrounding each Golgi apparatus.
(J) Quantification of the percentage of Golgi apparatus presenting anastomosis.
Each point in (C)–(F) represents an embryo (WT: n = 5 embryos from 3 litters, with 3–6 cells analyzed per embryo; *HeCo*: n = 4 embryos from 2 litters, with 2–11 cells analyzed per embryo). Data in (D) and (F) are normalized by the apical process length to avoid bias due to interkinetic nuclear migration. Each point in (H)–(J) represents an embryo (n = 3 embryos per condition from 3 litters, with 4–12 cells analyzed per embryo). Statistical test performed considering frequency across cells analyzed (J). Scale bars, 10 μm (A) and 0.5 μm (G). Data are represented as mean ± SEM and unpaired t test (C, D, F, H, and I) or median ± minimum-maximum range and Fisher's exact test (E and J). ****$p < 0.0001$, ***$p < 0.001$, and **$p < 0.01$.
See also Figure S4.

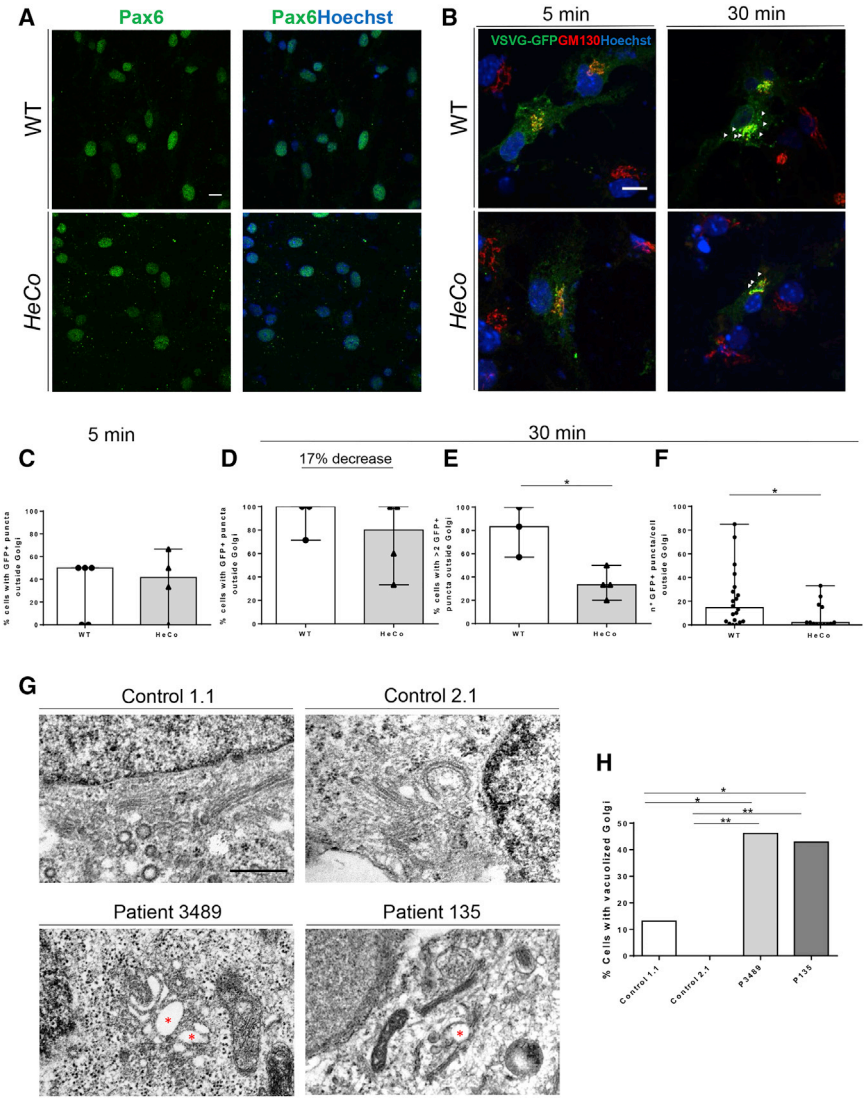

Figure 7. Golgi Anterograde Trafficking Is Perturbed in *Eml1* Mutant Progenitors *In Vitro*, and This Organelle Is Also Disrupted in iPSC-Derived Cortical Progenitors

(A) Pax6 (green) immunostaining in primary cultures of mouse neuronal progenitors from WT and HeCo mice (E13.5).

(B) Neuronal progenitor cells were transfected with VSVG-EGFP and incubated at 39°C. They were then incubated at 32°C and fixed 5 or 30 min later. Immunostaining with GM130 (red) was performed.

(C) Percentage of cells containing GFP^+ puncta outside the Golgi at 5 min.

(D) Percentage of cells containing GFP^+ puncta outside the Golgi at 30 min.

(E) Percentage of cells containing >2 GFP^+ puncta per cell outside the Golgi at 30 min.

(F) Number of GFP^+ puncta per cell outside the Golgi at 30 min.

(G) Representative EM images of the Golgi apparatus in cortical progenitors derived from control or EML1 patient iPSCs. Red asterisk shows vacuolized Golgi apparatus.

(H) Quantification of the percentage of Golgi apparatuses containing vacuolized Golgi. 20–28 cells were analyzed for each condition.

Cultures in (C)–(F) are from at least 3 embryos from 2 litters (n = 13–19 cells per condition). Each point in (C)–(E) represents an independent experiment. Statistical tests were performed considering the frequency across cells analyzed. Each point in (F) represents a cell. Scale bars, 10 μm (A and B) and 0.5 μm (G). Data are represented as median ± minimum-maximum range with Fisher's exact test (C, D, E, and H) or Mann-Whitney test (F). $^{**}p < 0.01$, and $^{*}p < 0.05$.

See also Figure S5.

mutations in this gene, which was previously only associated with Joubert and Meckel syndromes (Wiegering et al., 2018). It is likely that the heterotopia phenotype reflects the consequence of specific compound heterozygous mutations localized within the RPGR-interacting domain (RID) of the protein. Heterotopia mutations alter the interaction of RPGRIP1L with EML1 suggesting a convergent role for mutations in these proteins in SH pathophysiology. Overexpression of individual *RPGRIP1L* mutations also changes their subcellular localization and perturbs $Pax6^+$ progenitor organization in the mouse brain. Furthermore, *EML1* and *RPGRIP1L* patient fibroblasts show similar primary cilia assembly defects. Thus, multiple indications link these gene phenotypes.

Severe defects were identified in the centrosome-primary cilium complex in *HeCo* aRGs, as well as in *EML1* patient fibroblasts and cortical progenitor cells *in vitro*. These microtubule-based organelles are known to be critical for regulating aRG behavior, and when altered, severe brain and/or cortical malformations can arise (Bizzotto and Francis 2015). Centrosomal proteins are mostly associated with microcephaly (Bizzotto and Francis, 2015; Uzquiano et al., 2018), while defects in primary cilia have been associated with microcephaly, polymicrogyria, periventricular heterotopia (PV), focal cortical dysplasia, and ciliopathies (Ding et al., 2019; Gabriel et al., 2016; Kheradmand Kia et al., 2012; Park et al., 2018; Sheen et al., 2004). Of interest, certain rare mutations in OFD1, localized in the basal body and involved in primary cilium formation, have been previously associated with SH (Del Giudice et al., 2014). Our study further links the primary cilium to severe heterotopia conditions in mouse and human. Additionally, this is one of the few studies linking abnormal primary cilia to epilepsy (Canning et al., 2018; Park et al., 2018), a condition also suffered by patients with *EML1* mutations.

Although this study focused on aRGs, it is also important to study Eml1/EML1 function and primary cilia in other neocortical progenitors, which may contribute to the pathology. Our preliminary data concerning Arl13b distribution throughout the cortical wall in *HeCo* brains suggest potential abnormalities in more basal cortical regions likely to contain intermediate progenitors. We have also shown previously that *EML1* is expressed in the

SVZ of the gyrencephalic ferret brain (Kielar et al., 2014), and a more recent study confirmed its expression in basal RGs present in this zone in the human developing cortex (Nowakowski et al., 2017). Basal RG progenitors are thought to be crucial for neocortical expansion and gyrification and may be affected in severe cortical malformations (e.g., Bershteyn et al., 2017). It would thus be relevant to study EML1 and cilia function in this cell type.

Related to EML1 location and subcellular function, we did not identify its expression within the primary cilium in interphase cells. We hence investigated the molecular and cellular mechanisms that might be upstream of its insertion in the apical plasma membrane. Searching for additional interactors, we identified an appealing list of candidate partners that may play a role in the phenotype. We focused on the Golgi apparatus, since cargo sorting and trafficking are known to be critical for the correct formation of the centrosome-primary cilium complex (Bernabé-Rubio and Alonso, 2017; Madhivanan and Aguilar, 2014). In addition to VCIP135, other Golgi-related proteins identified by MS were shown to co-localize with this organelle (e.g., CK1δ); be important for its structure, morphology, and function (e.g., Scyl1, Map4, Camsap3, and Clasp1/2); or mediate cilia-targeted protein transport (e.g., Arf4). It is worth noting that some MS partners also showed ciliary localization and/or functions (e.g., Nup98 and Neurl4), and some were even reported to be localized both in the Golgi and in the centrosome-primary cilium (e.g., CK1δ, Map4, and Usp9x) and be important for their structure and/or function (e.g., Staufen2, KifC1, Kif7, and Macf1). Of note, Rpgrip1l appears also to be partially localized outside the cilia (Sang et al., 2011).

An interaction of EML1 with the Golgi protein VCIP135 was confirmed by heterologous expression in Neuro2A cells. The EML1 T243A patient missense mutation perturbs this interaction, as well as the interaction with the ciliary protein RPGRIP1L. To further confirm that aRG delamination in mutant conditions is related to these reduced interactions, rescue experiments with WT and mutant EML1 protein could be performed.

VSVG data also point toward a cargo sorting and/or trafficking defect in *HeCo* Pax6^{+} cells *in vitro*. Furthermore, the Golgi apparatus in *Eml1*/*EML1* mutant conditions shows an abnormal distribution and structure in mouse aRGs, patient fibroblasts, and human cortical progenitor cells. We hence have convincing cumulative evidence that this organelle normally requires Eml1/EML1 in these cell types. Correct Golgi-derived function is also critical for primary cilium formation (Bernabé-Rubio and Alonso, 2017; Madhivanan and Aguilar, 2014), which leads us to suggest that these Golgi phenotypes may be upstream of the centrosome-primary cilium defect identified in *Eml1*/*EML1* mutant conditions.

Previous studies have tentatively associated Golgi defects with cortical migration malformations, such as *ARFGEF2* mutations leading to microcephaly and PV (Sheen et al., 2004) and *DYNC1H1* mutations mainly leading to posterior pachygyria, polymicrogyria, and microcephaly (Schiavo et al., 2013). However, experiments reporting Golgi apparatus anomalies in the context of mutations in these two proteins were performed *in vitro* and not directly in neuronal progenitor cells (Fiorillo et al., 2014; Jaarsma and Hoogenraad, 2015; Sheen et al., 2004). Instead, we assessed the Golgi in neuronal progenitor cells (human and mouse), including in mouse aRGs *in vivo*, and were able to link Golgi anomalies to the pathogenesis of severe SH.

It remains to be elucidated if the Golgi functions altered in *Eml1*/*EML1* mutant conditions impact exclusively the centrosome-primary cilium pathway. If Golgi-dependent protein transport is more widely perturbed, then it could also affect the delivery of key adherens junction components to the plasma membrane, which is crucial for aRG polarity and behavior (Sheen et al., 2004; Uzquiano et al., 2018). This could loosen cell contacts between aRGs, allowing their delamination and contributing to the ectopic progenitor phenotype. Further experiments are thus required to understand the possible mechanisms related to Golgi-plasma membrane phenotypes in *Eml1*/*EML1* mutant conditions, as well as in other cortical malformation models.

Several signaling pathways integrated by the primary cilium (i.e., mTOR, Shh, Hippo, and Wnt; Wheway et al., 2018) might be expected to be disrupted in *Eml1*/*EML1* mutant conditions. For instance, changes in the mTOR signaling pathway have been previously associated with diverse pathological cortical phenotypes (Benova and Jacques, 2019; D'Gama et al., 2017; Foerster et al., 2017; Park et al., 2018). However, we did not find changes in this pathway in the *HeCo* telencephalon during the early-mid corticogenesis (data not shown). We also did not find any major changes in Shh signaling in *HeCo* dorsal telencephalon extracts during the same stages. Nevertheless, other approaches examining these pathways in aRGs specifically would be necessary to completely rule out their implication in the onset of the ectopic progenitor and thus heterotopia phenotype.

Assessing other pathways known to be mediated by the primary cilium could also help shed light on the downstream pathological mechanisms contributing to progenitor phenotypes. Another pathway associated with the primary cilium is the Hippo pathway (Wheway et al., 2018), although the relationship remains relatively unexplored. This pathway is known to regulate tissue homeostasis and hence to regulate cell growth, size, and shape (Ma et al., 2019). Primary cilium defects combined with changes in apical domain and endfeet features, as well as metaphase cell shape (this study; Bizzotto et al., 2017) make this pathway an appealing candidate underlying abnormal VZ dynamics in *Eml1* mutant conditions. Mutations in proteins involved in Hippo signaling have been previously associated with cortical malformations (Cappello et al., 2013; O'Neill et al., 2018). A recent study in the mouse also reported changes in the levels of key Hippo pathway proteins in the VZ of a model for SH, largely phenocopying the *HeCo* mouse phenotype (Liu et al., 2018). Therefore, assessing this pathway in *Eml1* mutant conditions would shed further light on the molecular mechanisms downstream of the primary cilium aRG phenotype.

In this study, we focused on the role of Eml1/EML1 during interphase; however, this protein can play various roles during the cell cycle (Bizzotto et al., 2017). This is consistent with the extra-ciliary role of many proteins important for the centrosome-primary cilium (Hua and Ferland, 2018). Further studying the function of Eml1 and its ciliary protein partners during different stages of the cell cycle will shed further light on their multivalent roles in dividing cortical progenitors. During

interphase, our data are consistent with the fact that fewer Eml1 mutant aRG endfeet form cilia, potentially due to abnormal ciliary protein targeting. Eml1 mutant aRG processes are hence deficient, either through abnormal signaling or via weakened membrane attachments due to abnormal adhesion component trafficking. We propose that these mechanisms contribute to progenitor delamination, initiating a sequence of events leading to heterotopia.

STAR★METHODS

Detailed methods are provided in the online version of this paper and include the following:

- KEY RESOURCES TABLE
- LEAD CONTACT AND MATERIALS AVAILABILITY
- EXPERIMENTAL MODEL AND SUBJECT DETAILS
  - Animals
  - Human Cell Culture
  - Heterotopia Patients with Mutations in EML1
  - Clinical Phenotype of the Patient P700-5
  - Human Fibroblast Cultures
  - Generation of Human iPSCs and Thereof Derived Cortical Progenitors
  - Retina Epithelial Pigmented Cell Culture
  - Mouse Neuronal Progenitor Cell Culture
  - Neuro2A Cell Culture
  - Freestyle 293F Cell Culture
- METHOD DETAILS
  - En Face Immunohistochemistry and Imaging
  - Electron Microscopy
  - Exome Sequencing of Heterotopia Patients: Analyses of *RPGRIP1L* Mutations
  - Embryonic Cortex Lysate
  - hTERT RPE-1 Cell Transfection
  - Freestyle 293F Cell Transfection, Protein Purification, and Pull Down for Mass Spectrometry
  - Mass Spectrometry
  - Neuro2A Transfection, Co-immunoprecipitation
  - Western Blot
  - Mouse Progenitor Cell Culture Transfection
  - Immunocytochemistry
  - Shmir Design and RT-qPCR
  - In Utero Electroporation
  - BrdU Injections and Immunohistochemistry
- QUANTIFICATION AND STATISTICAL ANALYSIS
  - En Face Imaging
  - Electron Microscopy
  - Immunohistochemistry and Immunocytochemistry Images
  - Immunoprecipitation and Western Blot
  - Statistical Analyses
- DATA AND CODE AVAILABILITY

SUPPLEMENTAL INFORMATION

Supplemental Information can be found online at https://doi.org/10.1016/j.celrep.2019.06.096.

ACKNOWLEDGMENTS

We thank Dr. M. Nosten-Bertrand for advice with statistical analyses and Dr. M. Stouffer, Dr. S. Bizzotto, Dr. A. Andreu-Cervera, G. Martinez Lorenzana, and A. Muzerelle for experimental help. We thank G. Arras from the LSMP for his assistance in MS data analysis and Dr. A. Houdusse for her advice. We thank Dr. A. Shihavuddin for his help with *en face* imaging data analysis. We are grateful to the following people for kindly gifting us materials and sharing protocols: Dr. C. Delevoye (TGN46 antibody), Dr. B. Goud (VSVG-GFP construct), Dr. A. Baffet (RPE1 cells and neuronal progenitor cell culture), Dr. V. Marthiens (neuronal progenitor cell culture), Dr. X. Zhang (FLAG-VCIP135 construct), Dr. M. Richards and Dr. R. Bayliss (Strep-YFP-EML1 construct), Dr. C. Lebrand (CAG-Tomato vector), Dr. F. Murakami (pCAG-Galt-EGFP construct), Dr. F. Watrin (small hairpin RNA [shmiRNA] empty vector), Dr. H. Lickert (Arl13b-RFP construct), and Dr. S. Schneider-Maunoury (c-myc-RPGRIP1L construct and Shh pathway antibodies). We thank the animal experimentation facility and cellular and tissue imaging platforms at the Institut du Fer à Moulin, supported also by the Région Ile de France and the FRC Rotary. We thank Dr. A. Croquelois for original mice, G. Grannec (IFM) and the TAAM (CDTA Orleans) for the maintenance of the *HeCo* mouse line. For patient sample provision and sequencing, we thank Mélanie Jennesson Lyve and Jacques Motte (Reims Hospital), Anne-Gaelle le Moing (Amiens Hospital), the Institut Imagine Biobank, Jamel Chelly (IGBMC, Strasbourg), Robert Olaso, Jean-Baptist Petit and Vincent Meyer (CNRGH, Evry), and Mara Cavallin and Karine Poirier (Institut Imagine, Paris) for their very helpful support, and all families for kindly agreeing to provide samples. A.U., D.M.R., A.H., and F.F. are associated with the BioPsy Labex project and the Ecole des Neurosciences de Paris Ile-de-France (ENP) network. Our salaries and labs were supported by Inserm; Centre National de la Recherche Scientifique (CNRS); Sorbonne University; French Agence National de la Recherche (ANR-13-BSV4-0008-01 and ANR-16-CE16-0011-03 to F.F. and N.B.-B.); Fondation Bettencourt Schueller (F.F.); the European Union (EU-HEALTH-2013, DESIRE, number 60253 to F.F. and N.B.-B.); the ERA-Net NEURON JTC 2015 Neurodevelopmental Disorders program affiliated with the ANR (for NEURON8-Full-815-006 STEM-MCD to F.F., N.B., and J.L.); the Fondation Maladies Rares/Phenomin (project IR4995 to F.F.); the European Cooperation in Science and Technology (COST Action CA16118 to G.M.S.M., N.B.-B., and F.F.); and the Hector Foundation II (to J.L.). This project was further supported by the French ANR under the frame of E-Rare-3, the ERA-Net for Research on Rare Diseases (ERARE18-049). A.U. received an ENP PhD grant and a Company of Biologists travel grant and was also funded by the Fondation de France (Prix Valérie Chamaillard, selected by the Fondation Française pour la Recherche sur l'Epilepsie). D.L. was supported by Région Ile-de-France (2013-2-EML-02-ICR-1) and Fondation pour la Recherche Médicale (DGE20121125630) grants.

AUTHOR CONTRIBUTIONS

A.U. conceived, designed, and performed experiments, analyzed data, and wrote the manuscript. C.C.-D. performed electron microscope experiments and data analyses. A.J. performed iPSC-derived neuronal progenitor cell cultures under the supervision of J.L. D.M.R. contributed to identification of the mutated gene for the P700 family and performed experiments. A.H. performed biochemistry experiments. F.D. carried out the MS experimental work, and D.L. supervised MS and data analysis. A.B. and J.-F. D. performed exome-sequencing experiments. C.M. contributed to confirmation of *RPGRIP1L* gene mutations under the supervision of N.B.-B. G.M.S.M. provided P3489 fibroblasts and contributed to cilia discussions. F.F. conceived and designed experiments, helped with data interpretation, and wrote the manuscript.

DECLARATION OF INTERESTS

The authors declare no competing interests.

Received: February 21, 2019
Revised: May 31, 2019
Accepted: June 27, 2019
Published: July 30, 2019

REFERENCES

Aigouy, B., Farhadifar, R., Staple, D.B., Sagner, A., Röper, J.C., Jülicher, F., and Eaton, S. (2010). Cell flow reorients the axis of planar polarity in the wing epithelium of Drosophila. Cell *142*, 773–786.

Alterio, J., Masson, J., Diaz, J., Chachlaki, K., Salman, H., Areias, J., Al Awabdh, S., Emerit, M.B., and Darmon, M. (2015). Yif1B is involved in the anterograde traffic pathway and the Golgi architecture. Traffic *16*, 978–993.

Ban, H., Nishishita, N., Fusaki, N., Tabata, T., Saeki, K., Shikamura, M., Takada, N., Inoue, M., Hasegawa, M., Kawamata, S., and Nishikawa, S. (2011). Efficient generation of transgene-free human induced pluripotent stem cells (iPSCs) by temperature-sensitive Sendai virus vectors. Proc. Natl. Acad. Sci. USA *108*, 14234–14239.

Benova, B., and Jacques, T.S. (2019). Genotype-phenotype correlations in focal malformations of cortical development: a pathway to integrated pathological diagnosis in epilepsy surgery. Brain Pathol. *29*, 473–484.

Bergmann, J.E. (1989). Using temperature-sensitive mutants of VSV to study membrane protein biogenesis. Methods Cell Biol. *32*, 85–110.

Bernabé-Rubio, M., and Alonso, M.A. (2017). Routes and machinery of primary cilium biogenesis. Cell. Mol. Life Sci. *74*, 4077–4095.

Bershteyn, M., Nowakowski, T.J., Pollen, A.A., Di Lullo, E., Nene, A., Wynshaw-Boris, A., and Kriegstein, A.R. (2017). Human iPSC-derived cerebral organoids model cellular features of lissencephaly and reveal prolonged mitosis of outer radial glia. Cell Stem Cell *20*, 435–449.e434.

Besse, L., Neti, M., Anselme, I., Gerhardt, C., Rüther, U., Laclef, C., and Schneider-Maunoury, S. (2011). Primary cilia control telencephalic patterning and morphogenesis via Gli3 proteolytic processing. Development *138*, 2079–2088.

Bizzotto, S., and Francis, F. (2015). Morphological and functional aspects of progenitors perturbed in cortical malformations. Front. Cell. Neurosci. *9*, 30.

Bizzotto, S., Uzquiano, A., Dingli, F., Ershov, D., Houllier, A., Arras, G., Richards, M., Loew, D., Minc, N., Croquelois, A., et al. (2017). Eml1 loss impairs apical progenitor spindle length and soma shape in the developing cerebral cortex. Sci. Rep. *7*, 17308.

Bustin, S.A., Benes, V., Garson, J.A., Hellemans, J., Huggett, J., Kubista, M., Mueller, R., Nolan, T., Pfaffl, M.W., Shipley, G.L., et al. (2009). The MIQE guidelines: minimum information for publication of quantitative real-time PCR experiments. Clin. Chem. *55*, 611–622.

Canning, P., Park, K., Gonçalves, J., Li, C., Howard, C.J., Sharpe, T.D., Holt, L.J., Pelletier, L., Bullock, A.N., and Leroux, M.R. (2018). CDKL family kinases have evolved distinct structural features and ciliary function. Cell Rep. *22*, 885–894.

Cappello, S., Gray, M.J., Badouel, C., Lange, S., Einsiedler, M., Srour, M., Chitayat, D., Hamdan, F.F., Jenkins, Z.A., Morgan, T., et al. (2013). Mutations in genes encoding the cadherin receptor-ligand pair DCHS1 and FAT4 disrupt cerebral cortical development. Nat. Genet. *45*, 1300–1308.

Croquelois, A., Giuliani, F., Savary, C., Kielar, M., Amiot, C., Schenk, F., and Welker, E. (2009). Characterization of the HeCo mutant mouse: a new model of subcortical band heterotopia associated with seizures and behavioral deficits. Cereb. Cortex *19*, 563–575.

D'Gama, A.M., Woodworth, M.B., Hossain, A.A., Bizzotto, S., Hatem, N.E., LaCoursiere, C.M., Najm, I., Ying, Z., Yang, E., Barkovich, A.J., et al. (2017). Somatic mutations activating the mTOR pathway in dorsal telencephalic progenitors cause a continuum of cortical dysplasias. Cell Rep. *21*, 3754–3766.

Del Giudice, E., Macca, M., Imperati, F., D'Amico, A., Parent, P., Pasquier, L., Layet, V., Lyonnet, S., Stamboul-Darmency, V., Thauvin-Robinet, C., and Franco, B. (2014). CNS involvement in OFD1 syndrome: a clinical, molecular, and neuroimaging study. Orphanet J. Rare Dis *9*, 74.

Delous, M., Baala, L., Salomon, R., Laclef, C., Vierkotten, J., Tory, K., Golzio, C., Lacoste, T., Besse, L., Ozilou, C., et al. (2007). The ciliary gene RPGRIP1L is mutated in cerebello-oculo-renal syndrome (Joubert syndrome type B) and Meckel syndrome. Nat. Genet. *39*, 875–881.

Ding, W., Wu, Q., Sun, L., Pan, N.C., and Wang, X. (2019). Cenpj regulates cilia disassembly and neurogenesis in the developing mouse cortex. J. Neurosci. *39*, 1994–2010.

Fiorillo, C., Moro, F., Yi, J., Weil, S., Brisca, G., Astrea, G., Severino, M., Romano, A., Battini, R., Rossi, A., et al. (2014). Novel dynein DYNC1H1 neck and motor domain mutations link distal spinal muscular atrophy and abnormal cortical development. Hum. Mutat. *35*, 298–302.

Foerster, P., Daclin, M., Asm, S., Faucourt, M., Boletta, A., Genovesio, A., and Spassky, N. (2017). mTORC1 signaling and primary cilia are required for brain ventricle morphogenesis. Development *144*, 201–210.

Fry, A.M., O'Regan, L., Montgomery, J., Adib, R., and Bayliss, R. (2016). EML proteins in microtubule regulation and human disease. Biochem. Soc. Trans. *44*, 1281–1288.

Gabriel, E., Wason, A., Ramani, A., Gooi, L.M., Keller, P., Pozniakovsky, A., Poser, I., Noack, F., Telugu, N.S., Calegari, F., et al. (2016). CPAP promotes timely cilium disassembly to maintain neural progenitor pool. EMBO J. *35*, 803–819.

Gaspard, N., Bouschet, T., Hourez, R., Dimidschstein, J., Naeije, G., van den Ameele, J., Espuny-Camacho, I., Herpoel, A., Passante, L., Schiffmann, S.N., et al. (2008). An intrinsic mechanism of corticogenesis from embryonic stem cells. Nature *455*, 351–357.

Gerhardt, C., Lier, J.M., Burmühl, S., Struchtrup, A., Deutschmann, K., Vetter, M., Leu, T., Reeg, S., Grune, T., and Rüther, U. (2015). The transition zone protein Rpgrip1l regulates proteasomal activity at the primary cilium. J. Cell Biol. *210*, 115–133.

Guo, J., Higginbotham, H., Li, J., Nichols, J., Hirt, J., Ghukasyan, V., and Anton, E.S. (2015). Developmental disruptions underlying brain abnormalities in ciliopathies. Nat. Commun. *6*, 7857.

Higginbotham, H., Guo, J., Yokota, Y., Umberger, N.L., Su, C.Y., Li, J., Verma, N., Hirt, J., Ghukasyan, V., Caspary, T., and Anton, E.S. (2013). Arl13b-regulated cilia activities are essential for polarized radial glial scaffold formation. Nat. Neurosci. *16*, 1000–1007.

Hua, K., and Ferland, R.J. (2018). Primary cilia proteins: ciliary and extraciliary sites and functions. Cell. Mol. Life Sci. *75*, 1521–1540.

Iefremova, V., Manikakis, G., Krefft, O., Jabali, A., Weynans, K., Wilkens, R., Marsoner, F., Brändl, B., Müller, F.J., Koch, P., and Ladewig, J. (2017). An organoid-based model of cortical development identifies non-cell-autonomous defects in Wnt signaling contributing to Miller-Dieker syndrome. Cell Rep. *19*, 50–59.

Jaarsma, D., and Hoogenraad, C. (2015). Cytoplasmic dynein and its regulatory proteins in Golgi pathology in nervous system disorders. Front. Neurosci *9*, 397.

Jung, B., Padula, D., Burtscher, I., Landerer, C., Lutter, D., Theis, F., Messias, A.C., Geerlof, A., Sattler, M., Kremmer, E., et al. (2016). Pitchfork and Gprasp2 target Smoothened to the primary cilium for Hedgehog pathway activation. PLoS ONE *11*, e0149477.

Kheradmand Kia, S., Verbeek, E., Engelen, E., Schot, R., Poot, R.A., de Coo, I.F.M., Lequin, M.H., Poulton, C.J., Pourfarzad, F., Grosveld, F.G., et al. (2012). RTTN mutations link primary cilia function to organization of the human cerebral cortex. Am. J. Hum. Genet. *91*, 533–540.

Kielar, M., Tuy, F.P., Bizzotto, S., Lebrand, C., de Juan Romero, C., Poirier, K., Oegema, R., Mancini, G.M., Bahi-Buisson, N., Olaso, R., et al. (2014). Mutations in Eml1 lead to ectopic progenitors and neuronal heterotopia in mouse and human. Nat. Neurosci. *17*, 923–933.

Kimura, T., and Murakami, F. (2014). Evidence that dendritic mitochondria negatively regulate dendritic branching in pyramidal neurons in the neocortex. J. Neurosci. *34*, 6938–6951.

Lamprecht, M.R., Sabatini, D.M., and Carpenter, A.E. (2007). CellProfiler: free, versatile software for automated biological image analysis. Biotechniques *42*, 71–75.

Li, A., Saito, M., Chuang, J.Z., Tseng, Y.Y., Dedesma, C., Tomizawa, K., Kaitsuka, T., and Sung, C.H. (2011). Ciliary transition zone activation of

phosphorylated Tctex-1 controls ciliary resorption, S-phase entry and fate of neural progenitors. Nat. Cell Biol. *13*, 402–411.

Lien, W.H., Klezovitch, O., Fernandez, T.E., Delrow, J., and Vasioukhin, V. (2006). alphaE-catenin controls cerebral cortical size by regulating the hedgehog signaling pathway. Science *311*, 1609–1612.

Liu, W.A., Chen, S., Li, Z., Lee, C.H., Mirzaa, G., Dobyns, W.B., Ross, M.E., Zhang, J., and Shi, S.H. (2018). PARD3 dysfunction in conjunction with dynamic HIPPO signaling drives cortical enlargement with massive heterotopia. Genes Dev. *32*, 763–780.

Ma, S., Meng, Z., Chen, R., and Guan, K. (2019). The Hippo pathway: biology and pathophysiology. Annu. Rev. Biochem *88*, 7.2–7.28.

Madhivanan, K., and Aguilar, R.C. (2014). Ciliopathies: the trafficking connection. Traffic *15*, 1031–1056.

Marthiens, V., Kazanis, I., Moss, L., Long, K., and Ffrench-Constant, C. (2010). Adhesion molecules in the stem cell niche–more than just staying in shape? J. Cell Sci. *123*, 1613–1622.

Mellacheruvu, D., Wright, Z., Couzens, A.L., Lambert, J.P., St-Denis, N.A., Li, T., Miteva, Y.V., Hauri, S., Sardiu, M.E., Low, T.Y., et al. (2013). The CRAPome: a contaminant repository for affinity purification-mass spectrometry data. Nat. Methods *10*, 730–736.

Nowakowski, T.J., Bhaduri, A., Pollen, A.A., Alvarado, B., Mostajo-Radji, M.A., Di Lullo, E., Haeussler, M., Sandoval-Espinosa, C., Liu, S.J., Velmeshev, D., et al. (2017). Spatiotemporal gene expression trajectories reveal developmental hierarchies of the human cortex. Science *358*, 1318–1323.

O'Neill, A.C., Kyrousi, C., Einsiedler, M., Burtscher, I., Drukker, M., Markie, D.M., Kirk, E.P., Gotz, M., Robertson, S.P., and Cappello, S. (2018). Mob2 insufficiency disrupts neuronal migration in the developing cortex. Front. Cell. Neurosci *12*, 57.

Palade, G.E. (1952). A study of fixation for electron microscopy. J. Exp. Med. *95*, 285–298.

Palmer, T.D., Willhoite, A.R., and Gage, F.H. (2000). Vascular niche for adult hippocampal neurogenesis. J. Comp. Neurol. *425*, 479–494.

Paridaen, J.T., Wilsch-Bräuninger, M., and Huttner, W.B. (2013). Asymmetric inheritance of centrosome-associated primary cilium membrane directs ciliogenesis after cell division. Cell *155*, 333–344.

Park, S.M., Lim, J.S., Ramakrishina, S., Kim, S.H., Kim, W.K., Lee, J., Kang, H.C., Reiter, J.F., Kim, D.S., Kim, H.H., and Lee, J.H. (2018). Brain somatic mutations in MTOR disrupt neuronal ciliogenesis, leading to focal cortical dysplamination. Neuron *99*, 83–97.e7.

Perez-Riverol, Y., Csordas, A., Bai, J., Bernal-Llinares, M., Hewapathirana, S., Kundu, D.J., Inuganti, A., Griss, J., Mayer, G., Eisenacher, M., et al. (2019). The PRIDE database and related tools and resources in 2019: improving support for quantification data. Nucleic Acids Res. *47* (*D1*), D442–D450.

Poullet, P., Carpentier, S., and Barillot, E. (2007). myProMS, a web server for management and validation of mass spectrometry-based proteomic data. Proteomics *7*, 2553–2556.

Richards, M.W., Law, E.W., Rennalls, L.P., Busacca, S., O'Regan, L., Fry, A.M., Fennell, D.A., and Bayliss, R. (2014). Crystal structure of EML1 reveals the basis for Hsp90 dependence of oncogenic EML4-ALK by disruption of an atypical β-propeller domain. Proc. Natl. Acad. Sci. USA *111*, 5195–5200.

Sang, L., Miller, J.J., Corbit, K.C., Giles, R.H., Brauer, M.J., Otto, E.A., Baye, L.M., Wen, X., Scales, S.J., Kwong, M., et al. (2011). Mapping the NPHP-JBTS-MKS protein network reveals ciliopathy disease genes and pathways. Cell *145*, 513–528.

Schiavo, G., Greensmith, L., Hafezparast, M., and Fisher, E.M. (2013). Cytoplasmic dynein heavy chain: the servant of many masters. Trends Neurosci. *36*, 641–651.

Shaheen, R., Sebai, M.A., Patel, N., Ewida, N., Kurdi, W., Altweijri, I., Sogaty, S., Almardawi, E., Seidahmed, M.Z., Alnemri, A., et al. (2017). The genetic landscape of familial congenital hydrocephalus. Ann. Neurol. *81*, 890–897.

Sheen, V.L., Ganesh, V.S., Topcu, M., Sebire, G., Bodell, A., Hill, R.S., Grant, P.E., Shugart, Y.Y., Imitola, J., Khoury, S.J., et al. (2004). Mutations in ARFGEF2 implicate vesicle trafficking in neural progenitor proliferation and migration in the human cerebral cortex. Nat. Genet. *36*, 69–76.

Shi, Y., Kirwan, P., Smith, J., Robinson, H.P., and Livesey, F.J. (2012). Human cerebral cortex development from pluripotent stem cells to functional excitatory synapses. Nat. Neurosci. *15*, 477–486, S1.

Sun, T., Wang, X.J., Xie, S.S., Zhang, D.L., Wang, X.P., Li, B.Q., Ma, W., and Xin, H. (2011). A comparison of proliferative capacity and passaging potential between neural stem and progenitor cells in adherent and neurosphere cultures. Int. J. Dev. Neurosci. *29*, 723–731.

Taverna, E., Mora-Bermúdez, F., Strzyz, P.J., Florio, M., Icha, J., Haffner, C., Norden, C., Wilsch-Bräuninger, M., and Huttner, W.B. (2016). Non-canonical features of the Golgi apparatus in bipolar epithelial neural stem cells. Sci. Rep. *6*, 21206.

Uchiyama, K., Jokitalo, E., Kano, F., Murata, M., Zhang, X., Canas, B., Newman, R., Rabouille, C., Pappin, D., Freemont, P., and Kondo, H. (2002). VCIP135, a novel essential factor for p97/p47-mediated membrane fusion, is required for Golgi and ER assembly in vivo. J. Cell Biol. *159*, 855–866.

Uzquiano, A., Gladwyn-Ng, I., Nguyen, L., Reiner, O., Gotz, M., Matsuzaki, F., and Francis, F. (2018). Cortical progenitor biology: key features mediating proliferation versus differentiation. J. Neurochem. *146*, 500–525.

Valot, B., Langella, O., Nano, E., and Zivy, M. (2011). MassChroQ: a versatile tool for mass spectrometry quantification. Proteomics *11*, 3572–3577.

Wang, L., Hou, S., and Han, Y.G. (2016). Hedgehog signaling promotes basal progenitor expansion and the growth and folding of the neocortex. Nat. Neurosci. *19*, 888–896.

Wheway, G., Nazlamova, L., and Hancock, J.T. (2018). Signaling through the primary cilium. Front. Cell Dev. Biol. *6*, 8.

Wiegering, A., Rüther, U., and Gerhardt, C. (2018). The ciliary protein Rpgrip1l in development and disease. Dev. Biol. *442*, 60–68.

Willaredt, M.A., Hasenpusch-Theil, K., Gardner, H.A., Kitanovic, I., Hirschfeld-Warneken, V.C., Gojak, C.P., Gorgas, K., Bradford, C.L., Spatz, J., Wölfl, S., et al. (2008). A crucial role for primary cilia in cortical morphogenesis. J. Neurosci. *28*, 12887–12900.

Wilson, S.L., Wilson, J.P., Wang, C., Wang, B., and McConnell, S.K. (2012). Primary cilia and Gli3 activity regulate cerebral cortical size. Dev. Neurobiol. *72*, 1196–1212.

Zhang, X., and Wang, Y. (2015). Cell cycle regulation of VCIP135 deubiquitinase activity and function in p97/p47-mediated Golgi reassembly. Mol. Biol. Cell *26*, 2242–2251.

Zhang, X., Zhang, H., and Wang, Y. (2014). Phosphorylation regulates VCIP135 function in Golgi membrane fusion during the cell cycle. J. Cell Sci. *127*, 172–181.

STAR★METHODS

KEY RESOURCES TABLE

REAGENT or RESOURCE	SOURCE	IDENTIFIER
Antibodies		
Mouse anti-γ tubulin	Sigma	T6557; RRID: AB_477584
Rabbit anti-Arl13b	Proteintech	17711-1-AP; RRID: 2060867
Mouse anti-GFP	Sigma	G6539; RRID: AB_259941
Rabbit anti-GFP	Invitrogen	A6455; RRID: AB_221570
Rabbit anti-Flag	Sigma	F7425, RRID: AB_439687
Mouse anti-Flag	Sigma	F1804; RRID: 262044
Mouse anti-c-myc	Cell Signaling Technology	9B11; RRID: AB_10889248
Mouse anti-Strep	Invitrogen	GT661; RRID: AB_2538749
Chicken anti-GAPDH	Millipore	AB2302; RRID: AB_10615768
Goat anti-Gli3	R&D systems	AF3690; AB_2232499
Alexa Fluor 633 Phalloidin	Thermo Fisher	A22284, N/A
Sheep anti-TGN46	BioRad	AHP500GT; RRID: AB_2203291
Mouse anti-GM130	BD Biosciences	Cat#610822; RRID: AB_10015242
Mouse anti-Sox2	R&D systems	MAB2018; RRID: AB_358009
Mouse anti-Pax6	Synaptic Systems	Cat#153011; RRID: AB_887758
Rabbit anti-Otx2	TaKaRa	M199, N/A
Rabbit anti-Foxg1	TaKaRa	M227, N/A
Rabbit anti-Arl13b	NeuroMab	Cat#75-287; RRID: AB_2341543
Mouse anti-Ki67	BD Biosciences	Cat#556003; RRID: AB_396287
Rat anti-BrdU	BioRad	MCA2060GA; RRID: AB_10545551
Chicken anti-GFP	Millipore	AB16901; RRID: 90890
Rabbit anti-Pax6	BioLegend	Cat#901301; AB2565003
Goat anti-mouse Alexa 488	Thermo Fisher	Cat#A28175; RRID: AB_2536161
Goat anti-rabbit Alexa 568	Thermo Fisher	Cat#A-11011; RRID: AB_143157
Dylight anti-mouse 800	Thermo Fisher	Cat#SA5-35521; RRID: AB_2556774
Dylight anti-rabbit 800	Thermo Fisher	Cat#SA5-35571; RRID: AB_2556775
Dylight anti-chicken 680	Thermo Fisher	Cat#SA5-10074; RRID: AB_2556654
Goat anti-mouse Alexa 568	Thermo Fisher	Cat#A-11031; RRID: AB_144696
Donkey anti-goat Alexa 568	Thermo Fisher	Cat#A-11057; RRID: AB_142581
Goat anti-rabbit Alexa 488	Thermo Fisher	Cat#A-11008; RRID: AB_143165
Goat anti-mouse Alexa 555	Thermo Fisher	Cat#A32727; RRID: AB_2633276
Goat anti-rat Alexa 568	Thermo Fisher	Cat#A-11006; RRID: AB_141373
Donkey anti-rabbit Alexa 647	Thermo Fisher	Cat#A-31573; RRID: AB_2536183
Bacterial and Virus Strains		
5-alpha competent E. coli	NEB	Cat#2988J
CytoTune-iPS 2.0 Sendai Reprogramming Kit	Thermo Fisher	A16517
Biological Samples		
Human fibroblasts	Coriell Biorepository	N/A
	Research center project SFB636 B7	
	Cell Bank Necker Hospital	
	Cell Bank Cochin Hospital	
	Erasmus Medial Center Cell Bank	

(*Continued on next page*)

Continued

REAGENT or RESOURCE	SOURCE	IDENTIFIER
Critical Commercial Assays		
QuikChange Lightning Site-Directed Mutagenesis kit	Agilent Technologies	Cat#210518
Lipofectamine 2000	Invitrogen	Cat#11668030
Lipofectamine 3000	Invitrogen	Cat#L3000001
Maxi prep kit	Macherey-Nagel	Cat#740410.10
NimbleGen chip 720,000-probes array	Roche-NimbleGen	N/A
SureSelect Human All Exon Kit v5	Agilent Technologies	N/A
Micro BCA Protein Assay Kit	ThermoFisher	Cat#23235
Polyethylenimine	Polysciences	Cat#23966-1
Strep-Tactin beads Superflow Plus	QIAGEN	Cat#30002
RSLCnano system	ThermoFisher	Ultimate 3000
Epoxy resin	PolySciences	EPON218
3500xL Genetic Analyzer for Human Identification	ThermoFisher	Cat#4406016
NanoViper Acclaim PepMap 100	ThermoFisher	N/A
5-bromo-2′-deoxyuridine (BrdU)	Sigma	B9285
Deposited Data		
PRIDE: PXD012714	Perez-Riverol et al., 2019	https://www.ebi.ac.uk/pride/archive/
Experimental Models: Cell Lines		
Human: hTERT RPE1	ATCC	N/A
Mouse: Neuro2A	ATCC	N/A
Human: FreeStyle 293	ATCC	N/A
Experimental Models: Organisms/Strains		
Mouse: HeCo NORCD1	Croquelois et al., 2009; Kielar et al., 2014	N/A
Mouse: Swiss	Janvier Labs	N/A
Oligonucleotides		
RPGRIP1L-ex24-R	This paper	5′ GCCTCCCAGGTATCTGGG 3′
RPGRIP1L-ex22-F	This paper	5′CAGTAGTGTACATTGCATTC 3′
RPGRIP1L-ex22-R	This paper	5′ TCTCTCTGTTCTTTCCACTTC 3′
RPGRIP1L-ex24-F	This paper	5′ CTTAGAAAGTGGATTAGTGTTC 3′
RM1_Vcpip1	KiCqStart, Sigma	5′ GGAAAAGTACAATGTTTGCC 3′
FW1_Vcpip1	KiCqStart, Sigma	5′ GCTACATTAATGGGAGAAGAC 3′
Recombinant DNA		
VSVts405-G-EGFP	B. Goud lab	N/A
CMV-3xFlag-EML1	Kielar et al., 2014	N/A
CMV-3xFlag-EML1 T243A	Kielar et al., 2014	N/A
pCAG-Galt-EGFP	Kimura and Murakami, 2014	N/A
pEGFP-C3-EML1	Kielar et al., 2014	N/A
pEGFP-C3-EML1 T243A	Kielar et al., 2014	N/A
pCS2-c-myc-RPGRIP1L	Delous et al., 2007	N/A
pCS2-c-myc-RPGRIP1L R1236C	This paper	N/A
pCS2-c-myc-RPGRIP1L V1188M	This paper	N/A
CMV-3xFlag-VCIP135	Zhang and Wang, 2015	N/A
pMAX-Strep-YFP-EML1	Richards et al., 2014	N/A
pCAGMIR30-shRNA scramble	This paper	5′ TCCTAATTTCCGTGTGACAGT 3′
pCAGMIR30-shRNA Vcip135	This paper	5′ TTGTGCCTCAGGACCTTATTA 3′
pMAX-Strep-YFP	This paper	N/A

(*Continued on next page*)

Continued

REAGENT or RESOURCE	SOURCE	IDENTIFIER
pCAGIG	Kielar et al., 2014, Addgene	N/A
pCAG-Arl13b-RFP	Jung et al., 2016	N/A
pCAG-IRES-Tomato	C. Lebrand lab	N/A
Software and Algorithms		
Prism	GraphPad software	N/A
Tissue Analyzer	Aigouy et al., 2010	https://imagej.nih.gov/ij/
Cell Profiler	Cell Profiler, Lamprecht et al., 2007	https://cellprofiler.org/
Fiji/ImageJ	Fiji/ImageJ	https://fiji.sc/
Unified Genotyper	GATK	https://software.broadinstitute.org/gatk/
Polyweb	University Paris Descartes Imagine Institute	N/A
Proteome discoverer version 2.1	ThermoFisher	N/A
MyProms	Poullet et al., 2007	N/A
MassChroQ version 1.2	Valot et al., 2011	N/A
CRAPome	Mellacheruvu et al., 2013	http://crapome.org/
Burrows Wheeler Aligner	SourceForge	https://sourceforge.net/projects/bio-bwa/files/
PolyPhen-2	PolyPhen-2	http://genetics.bwh.harvard.edu/pph2/
SIFT	Sorting Intolerant From Tolerant	https://sift.bii.a-star.edu.sg/

LEAD CONTACT AND MATERIALS AVAILABILITY

Further information and requests for resources and reagents should be directed to and will be fulfilled by the Lead Contact, Fiona Francis (**fiona.francis@inserm.fr**).

EXPERIMENTAL MODEL AND SUBJECT DETAILS

Animals

Research was conducted according to national and international guidelines (EC directive 2010/63/UE, French MESR 00984.02) with protocols followed and approved by the local ethical committee (Charles Darwin, Paris, France). *HeCo* mutant mice arose spontaneously in a colony of NOR-CD1 outbred stock, and selective inbreeding including crossing of living relatives and backcrossing were used to increase the occurrence of the phenotype in offspring as described in Croquelois et al., 2009. WT and *HeCo* mice derived from regularly crossed colonies were used for all the experiments described. The mode of inheritance of the phenotype is autosomal recessive. Normal, full-length transcripts of *Eml1* are absent in *HeCo* brains due to the insertion of an early retrotransposon (ETn) in the last intron of the gene, and are replaced by trace levels of shortened and chimeric Eml1-ETn transcripts (Kielar et al., 2014). Due to the lack of good Eml1 antibodies (8 different antibodies tested) we were unable to verify for residual abnormal protein. Timed-pregnant Swiss mice obtained from Janvier Labs (https://www.janvier-labs.com/) were used to prepare embryonic cortex lysates for mass spectrometry experiments as well as for *in utero* electroporation experiments. For staging of embryos, the day of vaginal plug was considered E0.5. Mice were housed with a standard 12 h light/dark schedule (lights on at 07:00 a.m.). Male and female embryos were used for all the experiments.

Human Cell Culture

Research on human cells was approved by the French Ministry of Health (L.1243.3, DC-2015-2559). The CIMH has ethical agreement for patient recruitment with respect to neurodevelopmental disorders and healthy controls. Patients involved were provided with detailed information about the study and gave written informed consent before being included in the study. All experiments with human material are in accordance with the declaration of Helsinki. The genetic analysis performed was subject to informed consent procedures and approved by the Institutional Review Boards at Necker Enfants Malades Hospital and Paris Descartes University.

Heterotopia Patients with Mutations in EML1

P135 and P3489 giant heterotopia male patients were as described in Kielar et al., 2014. R138X and T243A compound heterozygous *EML1* mutations were identified in patient P135. Homozygous W225R mutations were detected in patient P3489.

Clinical Phenotype of the Patient P700-5

P700-5 is a child of non-consanguineous Caucasian parents and was born at term with normal neonatal parameters. The patient was brought to medical attention at the age of 4, for developmental delay, secondary generalized focal seizures and left hemianopsia. During infancy, epilepsy became drug-resistant, with at least one seizure type consisting of left hemibody tonic seizure, with expression of fear, followed by left clonic movement for 30 s. Seizure frequency is up to 2 per day, in spite of multiple anti-epileptic drug combinations.

At last evaluation at 15 years of age, P700-5 presented moderate intellectual disability. He attended a specialized school, was able to read and write fluently, although showed difficulties in memorization. P700-5 is right handed. On examination, he demonstrated left hemiplegia, is able to walk but is extremely fatigable, and so uses a wheelchair in everyday life. He shows impaired oculo-manual coordination with oculo-cephalic apraxia associated with left hemianopsia.

On MRI performed at the age of 7 years, 7 months, P700-5 showed right subcortical heterotopia spanning the whole right hemisphere, surrounded by fronto-parieto temporal polymicrogyria, associated with almost complete corpus callosum agenesis and cerebellar dysplasia affecting the superior cerebellar vermis (Table S2).

Human Fibroblast Cultures

Skin biopsies were obtained with consent to isolate dermal fibroblasts using standard practices. Control 1 and control 2 have a male origin. Fibroblasts from P3489, P135 and P700-5 also have a male origin. Human fibroblasts were cultured in Dulbecco Modified Eagle Medium (DMEM) + GlutaMax (31966-021, Thermo Fisher) supplemented with 10% fetal bovine serum (FBS) and 50 μg/ml of primocin (Invivogen). Before splitting, the cells were washed with Hanks-Balanced Salt Solution (HBSS) followed by incubation for 3-5 minutes at 37°C with a 0.25% (w/v) Trypsin, 0.53 mM EDTA, PBS 1x solution. Then 3×10^4 cells were plated on 14 mm glass coverslips previously coated with Poly-L-Lysine 1x (PLL, Sigma Aldrich) O/N at 37°C, followed by extensive washing with sterile water. For serum starvation experiments, the cells were split, plated (3×10^4 in previously coated 14 mm coverslips) and cultured for 24h in complete medium. After 24h, the cells were cultured in the same medium without FBS.

Generation of Human iPSCs and Thereof Derived Cortical Progenitors

Skin fibroblasts were either obtained from the Coriell Biorepository (Ctrl2: catalog ID GM08680, male origin), or derived with given informed consent from a healthy donor within the collaborative research center project SFB636 B7 (Ctrl1: id-number B7_028#4, female origin) or from 2 well characterized EML1-patients (P3489 and P135, males, for more details see above and Kielar et al. [2014]). Fibroblasts were reprogrammed by non-integrative delivery of OCT4, SOX2, KLF4 and c-MYC using Sendai virus (SeV) vectors (Ban et al., 2011; Ethics Committee II of Heidelberg University approval no. 2009-350N-MA for hiPSC generation). Pluripotent stem cells were validated and maintained as described (Iefremova et al., 2017). In brief, pluripotency was confirmed by the expression of pluripotency-associated markers and three germ layer differentiation potential. The genomic integrity was validated by whole-genome single nucleotide polymorphism (SNP) genotyping and iPSCs were maintained under standard culture conditions.

Differentiation of iPSCs into cortical progenitors was performed as described with slight adaptations (Shi et al., 2012; Iefremova et al., 2017). In brief, iPSCs were cultured in PluriPro medium (Cell Guidance Systems). Once the cell culture reached 98% confluence, neural induction was initiated by changing the culture medium to neural induction media containing DMEM/F12 (N2 supplement, 1:50; B27 supplement, 1:50), cAMP (300 ng/ml, Sigma-Aldrich), LDN-193189 (0.5 μM, Miltenyi), A83-01 (0.21 μg, Miltenyi) and XAV939 (2μM, Enzo). Cells were maintained in this medium for 8–11 days, collected by dissociation with TrypL Express (Invitrogen) and replated in neural differentiation media containing DMEM/F12 (N2 supplement, 1:50; B27 supplement, 1:50) and cAMP (300 ng/ml, Sigma Aldrich) on Geltrex-coated (GT, Life Technologies) plastic dishes. Cortical identity was validated by marker expression. These cells homogeneously express the neural stem cell marker SOX2 as well as the forebrain markers FOXG1 and OTX2 and the dorsal marker PAX6 (Figure S3 E, see below). Cells were split in a 1:2 ratio when cultures reach 100% confluence using TrypL Express (Invitrogen). EM analyses were performed between passage one – three. See also Figure S3.

Retina Epithelial Pigmented Cell Culture

Retina Epithelial Pigmented (h-TERT RPE-1, female origin) cells were cultured in DMEM:F12 medium (30-2006, ThermoFisher) complemented with 10% FBS at 37°C and 5% CO_2. Before splitting the cells were washed with Hanks-Balanced Salt Solution (HBSS) followed by incubation for 3-5 minutes at 37°C with a 0.25% (w/v) Trypsin, 0.53 mM EDTA, 1 x PBS solution.

Mouse Neuronal Progenitor Cell Culture

The neuronal progenitor cell culture was adapted from Sun et al., 2011. Briefly, 6-well cell culture plates were coated with Poly-D-lysine (PDL, P6407, Sigma Aldrich) 2 $\mu g/cm^2$ in sterile 1 x PBS, O/N, at 37°C and 5% CO_2. The following day, the PDL was removed, and the plates were coated with 1 $\mu g/cm^2$ fibronectin (F1141, Sigma Aldrich) in sterile 1 x PBS. E13.5 timed-pregnant mice were sacrificed by cervical dislocation and the uterus was placed in ice cold basal medium (DMEM/F12 Hams, 21041, Thermo Fisher, 1% Pen-Strep (GIBCO), 2.9 mg/ml glucose and 1.2 mg/ml sodium bicarbonate). The embryos (males and females) were extracted from the uterus one by one and the cortex from both hemispheres was dissected and kept at 4°C in basal medium. The medium was removed and substituted by pre-warmed sterile complete medium (basal medium complemented with 1 x B27 without vitamin A (12589-010, GIBCO), 20 ng/ml of EGF (E9644, Sigma Aldrich) and 20 ng/ml of FGF (F0291, Sigma Aldrich). The tissue was dissociated

and each sample was centrifuged (3 min, 100 *rcf.*). The medium was removed and substituted by fresh pre-warmed complete medium followed by re-suspension of the cells. 1 × 10^5cells were plated in coated 6-well culture plates.

Neuro2A Cell Culture

Cells were cultured in 10% FBS-supplemented DMEM (ThermoFisher) at 37°C and 5% CO_2. Cells were dissociated with 0.025% trypsin–EDTA (25300-054, GIBCO) diluted in DMEM and plated into 100 mm Petri dishes (1 × 10^6/dish). Neuro2A cells have a male origin.

Freestyle 293F Cell Culture

293F cells were cultured in FreeStyle 293 Expression Medium (ThermoFisher), under constant agitation, at 37°C and 8% CO_2. These cells have a female origin.

METHOD DETAILS

En Face Immunohistochemistry and Imaging

En face immunohistochemistry (IHC) was performed as described in Bizzotto et al., 2017. F-actin immunodetection was performed to delineate cell boundaries (Marthiens et al., 2010), combined with centrosome and primary cilium markers (γ-tubulin and Arl13b, respectively), as a means of further identifying apical endfeet. Briefly, mouse embryonic brains were fixed in 4% w/v paraformaldehyde (PFA) (Sigma-Aldrich, France). Cortical explants were dissected and incubated 15 min at RT in PBST 1% (PBS 1X containing 1% Triton X-100 v/v and 0.02% sodium azide). Explants were then incubated 2 hours (h) at room temperature (RT) in blocking solution (PBS 1X, 0.3% Triton X-100 v/v, 0.02% sodium azide, 3% w/v Bovine Serum Albumin). Primary antibodies mouse anti-γ-tubulin (GTU-88, T6557, Sigma-Aldrich, 1:500) and rabbit anti-Arl13b (17711-1-AP, Proteintech, 1:500) were applied O/N at RT. After extensive washing in blocking solution, explants were incubated O/N at RT with secondary antibodies anti-mouse Alexa 488 and anti-rabbit Alexa 568 (1:1000, ThermoFisher) together with Hoechst (1:1000, ThermoFisher). Washes were performed in blocking solution and PBST 1%, and then the explants were incubated with Alexa Fluor 633 Phalloidin (1:100, Life Technologies) in PBST 1% O/N at RT. Extensive washing was performed in PBST 1% and PBS 1X before mounting the explants with Fluoromount G (Invitrogen) with the ventricular surface (VS) up to obtain an *en face* view of the ventricular side of the cortex. Fluorescently stained sections were imaged with a confocal TCS Leica SP5-II microscope.

Electron Microscopy

Mouse Embryos

Mouse embryos were transcardially perfused with a solution containing 4% PFA (Electron Microscopy Science), 2.5% glutaraldehyde in sodium phosphate buffer (PB) 0.1 M, pH 7.4. 3 h after perfusion, brains were dissected and post-fixed in the same solution O/N at 4°C. The samples were washed extensively with PB 0.1M, and afterward 3x 10 min washes with Palade buffer (Palade, 1952) were performed. The samples were incubated in 2% osmium tetroxide in Palade buffer for 40 min at RT, and then rinsed in Palade buffer for 3 min, followed by another 3 min wash in distilled water. They were dehydrated in a series of ethanol baths and flat-embedded in epoxy resin (EPON 812, Polysciences). After polymerization, blocks containing the dorsal telencephalon were cut at 70 nm thickness using an ultramicrotome (Ultracut E Leica). Sections were cut with a diamond knife and picked up on formvar-coated 200 mesh nickel one slot grids. Digital images were obtained with a CCD camera (Gatan Orius).

Human neuronal progenitor cells

Cells were fixed for 1 h in PB 0.1M buffer containing 4% PFA and 2.5% glutaraldehyde at 4°C. Following fixation, cells were postfixed in 2% osmium tetroxide diluted in 0.2M Palade buffer (Palade, 1952). After osmication, cells were dehydrated in a series of ethanol baths and flat-embedded in epoxy resin (EPON 812, Polysciences). After resin polymerization, small pieces were dissected from flat-embedded cultures, mounted in plastic stubs and sectioned. Ultrathin sections (70 nm) were stained with uranyl acetate and lead citrate. Sections were examined in a Philips CM100 electron microscope. Digital images were obtained with a CCD camera (Gatan Orius).

Exome Sequencing of Heterotopia Patients: Analyses of *RPGRIP1L* Mutations

Prior to exome analysis, for each patient, DNA was analyzed by CGH-microarray using the NimbleGen chip 720,000-probes (720 K) array (Roche-NimbleGen, Madison, WI) to exclude potential pathogenic CNVs.

Whole exome sequencing of peripheral blood DNA from the proband and both parents was performed using the Agilent SureSelect Human All Exon Kits v5, and sequences were generated on a HISeq2500 machine (Illumina). Sequences were aligned to hg19 by using BWA v.0.6.1, and single nucleotide variants (SNVs) and indels were called by using GATK v.1.3. Annotation of variants was performed with GATK Unified Genotyper. All calls with read coverage of ≤ 2 × or a Phred-scaled SNP quality score of ≤ 20 were removed from consideration. The annotation process was based on the latest release of the Ensembl database. Variants were annotated and analyzed using the Polyweb software interface designed by the Bioinformatics platform of University Paris Descartes and Imagine Institute.

Filters used for variant screening were as follows: (i) all variants previously observed (in dbSNP138 and/or in in-house projects) were excluded; (ii) only variants leading to abnormal protein sequence (splicing, non-synonymous, frameshift, stop) were retained;

(iii) we considered the PolyPhen-2 and SIFT prediction status as informative but not restrictive. Because the patient was a sporadic case from unrelated parents, the following models of inheritance in the variant screening were considered: autosomal recessive (in particular compound heterozygous but without excluding homozygous variants), X-linked and *de novo* SNVs.

A compound heterozygous mutation in *RPGRIP1L* was identified in a patient with subcortical heterotopia (P700; a c.3562G>A nucleotide mutation in exon 22 was transmitted from the mother and c.3706C>T nucleotide mutation in exon 24 was transmitted from the father, Table S1). Genomic DNA amplifications were performed for *RPGRIP1L* using standard procedures (RPGRIP1L-ex22-F: 5′CAGTAGTGTACATTGCATTC 3′ ; RPGRIP1L-ex22-R: 5′ TCTCTCTGTTCTTTCCACTTC 3′ ; RPGRIP1L-ex24-F: 5′ CTTA GAAAGTGGATTAGTGTTC 3′ ; RPGRIP1L-ex24-R: 5′ GCCTCCCAGGTATCTGGG 3′), and PCR products were analyzed by direct sequencing using an 3500xL Genetic Analyzer (Applied Biosystems, Foster City, CA).

Embryonic Cortex Lysate

For mass spectrometry experiments E13.5 timed-pregnant Swiss mice (Janvier Labs, France) were sacrificed by cervical dislocation. Embryos were dissected and both brain hemispheres collected in ice cold L-15 medium. Explants were immediately frozen in liquid nitrogen and ground into a powder. Hemispheres from different embryos were pooled. The powder was re-suspended in 10 μl/mg lysis buffer (Tris HCl 50 mM, NaCl 150 mM, EDTA 1 mM pH 8) supplemented with NP-40 1% and protease inhibitors 1x (Complete Protease Inhibitor Cocktail Tablets EDTA-Free, Roche). The lysate was homogenized by rotation during 45 min at 4°C, then centrifuged for 30 min at 15000 r*cf.* and 4°C. The supernatant was collected and stored at −80°C.

For western blot experiments designed to study the Shh signaling pathway the protocol was mildly modified. Once the cortex was dissected and fast-frozen in liquid nitrogen, lysis of each embryonic cortex (from both hemispheres) was performed individually, by re-suspending the tissue continuously with lysis buffer for a period of 2 h at 4°C. Then the lysate was centrifuged (30 min, 15000 r*cf.*, 4°C), the supernatant collected and protein concentration measured using the BCA Protein Assay Kit (Thermo Fisher) and the ELISA microplate reader BertholdTech Mithras.

hTERT RPE-1 Cell Transfection

6×10^4 cells were plated in previously coated 14 mm glass coverslips (PLL, 10 min RT, followed by extensive washing with sterile water). 24 h later, cells were transfected with a ratio of 1:4 DNA and lipofectamine 2000 (Invitrogen). 2 μl of lipofectamine were combined with 50 μl of OPTI-MEM Media (ThermoFisher). In parallel 0.5 μg of DNA were combined with 50 μl of OPTI-MEM. The latter solution was mixed with the former and after 20 min at RT, the mix was applied to the cells. 24 h after transfection the cells were fixed and immunostained (see below).

Freestyle 293F Cell Transfection, Protein Purification, and Pull Down for Mass Spectrometry

For transfection, 1×10^6 cells were cultured in a 125 mL Erlenmeyer. 45 μg of Polyethylenimine (PEI, Polysciences) were mixed with 750 μl of OPTI-MEM (ThermoFisher) and 22.5 μg of DNA with 750 μl of OPTI-MEM, for a 1:2 ratio of DNA: PEI. The DNA was mixed with the PEI solution and after a period of 10 min at RT the mix was applied to the cells. 72 h later the cells were recovered, washed with 1 x PBS and lysed with 750 μl of lysis buffer (Tris HCl 50 mM, NaCl 150 mM, EDTA 1 mM pH 8) supplemented with NP-40 1% and protease inhibitors 1X (Complete Protease Inhibitor Cocktail Tablets EDTA-Free, Roche). After 30 min of rotation at 4°C, the samples were centrifuged for 15 min, 14.000 r*cf.*, at 4°C. The supernatant was kept and protein content was measured with the BCA Protein Assay Kit (ThermoFisher) and the ELISA microplate reader BertholdTech Mithras, in order to ensure similar protein concentrations across the different conditions.

For protein purification, Strep-Tactin beads Superflow Plus (30002, QIAGEN) were used. 40 μl of beads previously washed with lysis buffer were used for each purified protein sample. They were incubated with 2 mg of protein lysate (in a 100 μl volume) for 1 h at 4°C under rotation. The samples were then centrifuged (3 min, 200 r*cf.*, 4°C), and the supernatant was kept as the 'unbound' fraction. The beads were washed (3x) with a more stringent lysis buffer containing 500 mM NaCl, in order to eliminate possible proteins binding to the beads in a non-specific fashion. For control experiments to check correct protein purification, elution was performed with NuPAGE LDS Buffer (ThermoFisher). For pull down samples to analyze by mass spectrometry (n = 4/condition), the Strep-Tactin beads already bound to the protein of interest (Strep-YFP or Strep-YFP-EML1) were incubated with 15 μg of cortex lysate (described above) O/N, at 4°C, under rotation. Then the samples were centrifuged (3 min, 200 r*cf.*, 4°C), and the 'unbound cortex' recovered. The beads containing the purified protein of interest and its interacting partners were extensively washed with lysis buffer (150 mM NaCl). They were stored at 4°C for mass spectrometry analyses.

Mass Spectrometry

Strep-Tactin beads containing the purified protein of interest and its interacting partners were washed twice with 100 μL of 25 mM NH_4HCO_3 and an on-bead digestion with 0.2 μg of trypsin/LysC (Promega) was performed for 1 h in 100 μL of 25 mM NH_4HCO_3. Samples were then loaded onto homemade C18 StageTips for desalting. Peptides were eluted using 40/60 MeCN/H_2O + 0.1% formic acid and vacuum concentrated to dryness. Samples were chromatographically separated using an RSLCnano system (Ultimate 3000, Thermo Scientific) coupled online to an Orbitrap Fusion Tribrid mass spectrometer (Thermo Scientific). Peptides were trapped on a C18 column (75 μm inner diameter × 2 cm; nanoViper Acclaim PepMap^{TM} 100, Thermo Scientific) with buffer A (2/98 MeCN/H_2O in 0.1% formic acid) at a flow rate of 4.0 μL/min over 4 min. Separation was performed on a 50 cm x 75 μm

C18 column (nanoViper Acclaim PepMap^{TM} RSLC, 2 μm, 100Å, Thermo Scientific) regulated to a temperature of 45°C with a linear gradient of 5% to 25% buffer B (100% MeCN in 0.1% formic acid) at a flow rate of 300 nL/min over 100 min. Full-scan MS was acquired in the Orbitrap analyzer with a resolution set to 120,000 and ions from each full scan were HCD fragmented and analyzed in the linear ion trap.

For identification, the data were searched against the mouse SwissProt database using Sequest HF through proteome discoverer version 2.1. Enzyme specificity was set to trypsin and a maximum of two-missed cleavage sites were allowed. Oxidized methionine, N-terminal acetylation, and carbamidomethyl cysteine were set as variable modifications. Maximum allowed mass deviation was set to 10 ppm for monoisotopic precursor ions and 0.6 Da for MS/MS peaks.

The resulting files were further processed using myProMS (Poullet et al., 2007). FDR calculation used Percolator and was set to 1% at the peptide level for the whole study. The label free quantification was performed by peptide Extracted Ion Chromatograms (XICs) computed with MassChroQ version 1.2 (Valot et al., 2011).

For protein quantification, XICs from proteotypic and non-proteotypic peptides shared between compared conditions (TopN matching) with no missed cleavages were used. Global MAD normalization was applied on the total signal to correct the XICs for each biological replicate. Protein ratios were computed as the geometrical mean of related peptides. To estimate ratio significance, a two-tailed *t test* was performed and *p-value*s were adjusted with a Benjamini–Hochberg FDR procedure with a control threshold set to 0.05.

A $\geq$ 1.5 fold-change and $\geq$ 3 peptides/protein were used as criteria to obtain a list of EML1 interacting partners (240). Further filtering was performed (nucleic acid-associated proteins) refining the list of EML1 protein partners (113).

Additionally, to check for the specificity of the list of proteins obtained, we used the CRAPome (Contaminant Repository for Affinity Purification, www.crapome.org), a depository that contains multiple negative controls from mass spectrometry experiments allowing to query the specificity of the proteins obtained in MS results (Mellacheruvu et al., 2013). Only 3.3% of the proteins were recognized as frequently found in the CRAPome data base, which ensures the specificity of the protein list.

Neuro2A Transfection, Co-immunoprecipitation

After 24 h in culture, cells reaching 70%–80% confluence were transfected using a ratio of 1:3 DNA and PEI, respectively (10 μg of DNA and 30 μg of PEI, Polysciences). The following constructs were used for co-immunoprecipitation experiments: pMAX-Strep-YFP-EML1, CMV-3xFlag-EML1, CMV-3xFlag-EML1 T243A, pEGFP-C3-EML1, pEGFP-C3-EML1 T243A, pCS2-c-*myc*-RPGRIP1L, pCS2-c-*myc*-RPGRIP1L R1236C, pCS2-c-*myc*-RPGRIP1L V1188M, pCMV-3xFlag-VCIP135 (Delous et al., 2007; Kielar et al., 2014; Zhang and Wang, 2015), and the corresponding control vectors. Site directed mutagenesis to obtain the c-*myc*-RPGRIP1L mutant constructs was performed with the QuikChange Lightning Kit (Agilent Technologies). To test the shmiRNA efficiency, the pCAGMIR30-shRNA scrambled and pCAGMIR30-shRNA Vcip135 constructs were transfected in Neuro2A cells.

For co-IPs, after 48 h, cells were recovered and washed twice with 1 X PBS and lysed by rotation for 20 min at 4°C in 150 μl of RIPA buffer (50 mM Tris-HCl, pH 8, 100 mM NaCl, 1 mM EDTA, 0.1% SDS, 1% Nonidet P-40, 0.5% sodium deoxycholate and protease inhibitor mix from Roche). The samples were centrifuged at 14000 *rcf.* for 15 min at 4°C. Protein G Sepharose beads (Sigma Aldrich) were diluted 1/10 in TNE buffer (50 mM Tris-HCl pH 7.4, 100 mM NaCl, 5 mM EDTA) and 60 μl of diluted beads were used for each IP experiment. The beads were extensively washed with 1 x RIPA buffer, followed by centrifugation (12000 *rcf.*, 4°C, 30 s). A pre-clearing step was performed by incubating the cell lysates with the already-washed beads in a rotating wheel at 4°C for 1 h 30 min. The samples were then centrifuged (12000 *rcf.*, 4°C, 30 s) and the supernatant collected. The latter was incubated with the following primary antibodies (1 μg): mouse anti-GFP (G6539, Sigma-Aldrich), rabbit anti-GFP (A6455, Invitrogen), rabbit anti-Flag (F7425, Sigma-Aldrich), mouse anti-Flag (F1804, Sigma Aldrich), mouse anti-c-*myc* (Cell Signaling Technology) and mouse anti-Strep (GT661, Invitrogen) (O/N, 4°, rotating wheel).

Afterward, these samples were incubated with 100 μl of diluted washed Protein G Sepharose beads (5 h, 4°C, rotating wheel). The unbound fraction was recovered after centrifugation (12000 *rcf.*, 4°C, 30 s). 5x washes of the beads in 1 x RIPA buffer were performed before elution with NuPAGE LDS Buffer (Thermo Fisher), 10 min at 70°C. The bound fraction was recovered after centrifugation (12000 *rcf.*, RT, 2 min).

Western Blot

Samples were denatured with 2x NuPAGE LDS Buffer (ThermoFisher) for 10 min at 70°C. Denaturing electrophoresis was performed on a 4%–12% Bis-Tris Gel with MOPS SDS running buffer for 2 h at 110V. Proteins were transferred onto nitrocellulose membranes for 2 h at 110V and 4°C in a Tris-Glycine transfer buffer (Tris 25 mM, Glycine 192 mM, ethanol 10%). After protein transfer, the membranes were stained with Ponceau S to check the transfer quality. This provided a loading control for the membranes revealing total protein amounts in each lane. The membranes were extensively washed with distilled water, followed by a 30 min incubation in TBST 1x (100 mM Tris pH 7.5, 150 mM NaCl, 10% ethanol, 0.05% Tween) supplemented with 5% milk. Incubation with the secondary antibody (see below) was performed to identify non-specific binding sites. Briefly, the antibody was incubated in the dark for 2h, and afterward extensive washes with TBST 1x were performed, prior to imaging (see below). The primary antibodies were then incubated O/N at 4°C with agitation or for a period of 2 h at RT. The following primary antibodies were used: goat anti-Gli3 (AF3690, R&D systems, 1:500), mouse anti-GFP (G6539, Sigma-Aldrich), rabbit anti-GFP (A6455, Invitrogen), rabbit anti-Flag (F7425, Sigma-Aldrich, 1:300), mouse anti-Flag (F1804, Sigma Aldrich, 1:500), mouse anti-c-*myc* (Cell Signaling Technology, 1:400), mouse anti-Strep

(GT661, Invitrogen, 1:1000), chicken anti-GAPDH (AB2302, Millipore, 1:10000). The membranes were extensively washed with TBST, followed by incubation with the secondary antibody: Dylight anti-mouse 800, anti-rabbit 800 and anti-chicken 680 (ThermoFisher, 1:10000). After extensive washes in TBST, the membranes were scanned using an Odyssey (Li-Cor) infrared scanner.

Mouse Progenitor Cell Culture Transfection

The cells were split once before performing transfection experiments. Half of the culture medium was changed by fresh complete medium every 2 days. For splitting, cells were washed with pre-warmed Versene (GIBCO), followed by a 3 min incubation with pre-warmed StemPro Accutase (GIBCO) at 37°C. Cells were plated (6-8 × 10^5) on coated 14 mm glass coverslips for transfection.

For transfections (VSVts405-G-EGFP, pCMV-3xFlag-Eml1, pCAG-Galt-EGFP), a ratio of 1:2:2 DNA with Lipofectamine 3000 and Lipofectamine 3000 Reagent was used. 1 μl of lipofectamine was mixed with 25 μl of OPTI-MEM, and 0.5 μg of DNA were mixed with 2 μl of lipofectamine reagent in 50 μl of OPTI-MEM. The latter solution was mixed with the former and after 5 min at RT the mix was applied to the cells.

For the VSVG experiments, cells were incubated at 39.5°C and 5% CO_2. 24 h later the cells were incubated at 32°C to allow the release of the VSVG protein. The cells were fixed 5 and 30 min afterward, and immunostained (see below).

Immunocytochemistry

Cells were washed in 1 x PBS prior to fixation with 4% w/v PFA in 0.1 M phosphate buffer, pH 7.4, for 15 min at RT. The cells were extensively washed in 1 x PBS followed by a 15 min wash in PBST 0.2% (Triton X-100 0.2% in 1 x PBS). Incubation with blocking solution (3% BSA, 0.2% Triton X-100 in 1 x PBS) was performed for 1 h at RT and the following primary antibodies were applied for 2 h at RT or O/N at 4°C: mouse anti-GFP (G6539, Sigma-Aldrich, 1:500), rabbit anti-Flag (F7425, Sigma-Aldrich, 1:500), mouse anti-γ-tubulin (GTU-88, T6557, Sigma-Aldrich, 1:500), rabbit anti-Arl13b (17711-1-AP, Proteintech, 1:500), sheep anti-TGN46 (AHP500GT, BioRad, 1:500), mouse anti-GM130 (610822, BD Biosciences, 1:300). The cells were extensively washed with PBST 0.2% and the following secondary antibodies were incubated combined with Hoechst (1:1000, ThermoFisher) for 45 min at RT in the dark: anti-mouse Alexa 488, anti-mouse Alexa 568, anti-rabbit Alexa 568, anti-goat Alexa 568 (1:1000, ThermoFisher). The cells were extensively washed in PBST 0.2% and the coverslips mounted with Fluoromount G (Southern Biotechnology). Images were acquired with a TCS Leica SP5-II confocal microscope.

For detection of the neural and/or cortical progenitor markers SOX2, PAX6, FOXG1 and OTX2 and the primary cilium marker ARL13B, cells were fixed for 10 min in 4% w/v PFA (Sigma-Aldrich), washed three times with PBS and transferred to blocking solution containing 10% FCS in PBS and 0.1% Triton X-100 for 1 h, incubated with the primary antibodies for 16 h at 4°C, washed three times with PBS, incubated for 1 h with secondary antibodies, counterstained with DAPI (BioLegend) and mounted with Mowiol 4-88. Antibodies and concentrations were as follows: mouse anti-Sox2 (MAB2018, R&D Systems, 1:500), Pax6 (153011, Synaptic Systems, 1:300), Otx2 (M199, TaKaRa, 1:400), FoxG1 (M227, TaKaRa, 1:400), Arl13b (75-287, NeuroMab, 1:50), anti-rabbit Alexa 488 (1:1000, ThermoFisher) and anti-mouse Alexa 555 (1:1000, ThermoFisher). Images were acquired with a Celldiscoverer 7 microscope (Zeiss).

Shmir Design and RT-qPCR

pCAGMIR30-shRNA (Addgene) scrambled and pCAGMIR30-shRNA Vcip135 were designed with the siRNA Wizard tool (Invivogen), sequences are respectively: 5′ TTGTGCCTCAGGACCTTATTA 3′ and 5′ TCCTAATTTCCGTGTGACAGT 3′. Total RNA samples were extracted from transfected Neuro2A cells (RNeasy protect mini kit, QIAGEN). First-strand cDNA was synthesized using oligo (dT) and the Superscript III Reverse Transcriptase kit (Invitrogen). Gene-specific primers were designed by KiCqStart SYBR green primers (Sigma Aldrich, primer set 1). The cyclophilin B (*Ppib*, peptidylpropyl isomerase B) and prosaposin (*Psap*) genes were used for normalization (geometric mean). Real-time qPCRs were performed using the SYBR green method, following MIQE guidelines (Bustin et al., 2009). Standard curves were generated from assays made with serial dilutions of cDNA to calculate PCR efficiencies (90% < efficiency < 105%, with r^2 > = 0.998). Threshold cycles (Ct) were transformed into quantity values using the formula $(1 + \text{efficiency})^{-Ct}$. Differential expression analyses were performed with Student t tests.

In Utero Electroporation

Timed-pregnant mice (E13) were anesthetized with isoflurane (4% during induction and 2%–2.5% during surgery) and embryos exposed within the intact uterine wall after sectioning the abdomen. Embryos were constantly hydrated with NaCl 0.9% (B. Braun). A solution containing DNA (1 μg/μl per plasmid) and 20% w/v fast green in sterile endo-free water was injected in the lateral ventricles of the embryos. Different combinations of plasmids were used of the following vectors: pCAGIG, pCAG-Arl13b-RFP (Jung et al., 2016), pCS2-c-*myc*-RPGRIP1L R1236C, pCS2-c-*myc*-RPGRIP1L V118M, pCAG-IRES-Tomato, pEGFP-C3-EML1, pCAG-Galt-EGFP (Kimura and Murakami, 2014), pCAGMIR30-shRNA scrambled and pCAGMIR30-shRNA Vcip135. Forceps electrodes (System CUY650P5 NepaGene Co) were placed around the embryo head at a 45° angle and plasmids electroporated by discharging a 4,000-μF capacitor charged to 35 V (five electric pulses of 50 ms with 500 ms intervals) with a CUY21 NepaGene electroporator. The embryos were then placed back in the abdominal cavity until a later developmental time point for subsequent analyses.

BrdU Injections and Immunohistochemistry

For cycling progenitor analyses at E12.5, pregnant females were injected with 5-bromo-2′-deoxyuridine (BrdU, 99% Bioultra, Sigma-Aldrich, 50 μg per gram body weight in NaCl 0.9%) and sacrificed after 30 min. Embryonic brains were fixed by immersion O/N at 4°C in 4% w/v PFA in 0.1 M phosphate buffer, pH 7.4, followed by extensive washes in 1 x PBS. Brains were cut in 70 μm thick coronal sections using a vibrating blade microtome (Leica VT1000 S). In order to perform immunohistochemistry combining the primary antibodies mouse anti-Ki67 (BD 556003, 1:200) and rat anti-BrdU (BioRad, MCA2060GA, 1:1000), antigen retrieval was performed by incubating the sections in sodium citrate 10 mM pH 6 at 95°C for 20 min and allowing them to cool before blocking. Blocking was performed for 1 h at RT with blocking solution (1X PBS with 10% Goat Serum and 0.5% Triton X-100) before incubation O/N at 4°C with the primary antibody (Ki67, proliferation marker). After extensive washes, sections were incubated with the secondary antibody anti-rabbit Alexa 488 (Life Technologies, 1:1000) for 2 h at RT. This was followed by a 10 min incubation in Hoechst (ThermoFisher, 1:1000) and then sections were fixed with 8% PFA w/v for 15 min at RT (Palmer et al., 2000). Extensive washes with PBST 0.1% (1X PBS and 0.1% Triton X-100) were performed, followed by incubation in 2N hydrochloric acid for 30 min at 37°C. After extensive washes, the sections were incubated with the primary antibody (BrdU), secondary antibody Alexa 568 (Life Technologies, 1:1000), Hoechst, and then mounted with Fluoromount G (Invitrogen).

Brain sections (50 μm thick) from *in utero* electroporation experiments related to Vcip135 were exclusively incubated with Hoechst and extensively washed before mounting. For other IHC experiments (brain sections 50-70 μm thick) the following primary antibodies were used: mouse anti-GFP (G6539, Sigma-Aldrich, 1:500), chicken anti-GFP (AB16901, Millipore, 1:500), rabbit anti-Pax6 (901301, BioLegend, 1:300), anti-Arl13b (17711-1-AP, Proteintech, 1:500) and secondary antibodies Alexa 488, Alexa-568 and Alexa-647 (ThermoFisher).

QUANTIFICATION AND STATISTICAL ANALYSIS

En Face Imaging

Images were acquired with a 0.17 μm z stack depth. At least two randomly-chosen ROIs (100 × 100 μm) were analyzed per embryo, and the analyzed images had a total depth of 1 μm. Images were analyzed using the ImageJ plugin Tissue Analyzer (Aigouy et al., 2010) and the publicly available software Cell Profiler (Lamprecht et al., 2007), a method previously described in Foerster et al., 2017.

Electron Microscopy

Images were analyzed using ImageJ.

Immunohistochemistry and Immunocytochemistry Images

Images were analyzed using ImageJ. For Ki67+BrdU+ cell distribution analyses, regions of interest (ROI) were selected from both hemispheres, spanning the whole cortical wall and with a width of 100 μm. Two ROIs were quantified per animal. The E12.5 cortical wall was divided in five equally-sized bins, bin 1 and 5 corresponding to the most apical (apical ventricular zone) and basal (cortical plate) regions of the developing cortex, respectively (Figure S1A). For *in utero* electroporation experiments and primary cilia (Arl13b+) distribution analyses (Figures S2D, S5A, and S1L, respectively), the E13.5 or E14 cortex was subdivided in 6-equally sized bins, bin 1 and 6 corresponding to the most apical (apical ventricular zone) and basal (cortical plate) regions of the developing cortex, respectively. Cells that were positive in each bin for the selected markers were quantified, and the percentage relative to the total number of positive cells across the cortical wall was compared between the two conditions in each different bin. For primary cilium analyses, the number of Arl13b+ cilia in each bin was quantified, normalized by the total number across the different bins.

For *in utero* electroporation experiments addressing Golgi apparatus localization in aRGs, individual electroporated Tomato+ cells were selected and analyzed. Similar parameters to the ones described in Taverna et al., 2016 were quantified.

For patient fibroblast primary cilium and Golgi apparatus analyses ImageJ was used. Axoneme length was measured manually using Arl13b immunodetections. Golgi analyses were performed with the plugin 3D Object Counter.

Images for all experiments were acquired with a TCS Leica SP5-II confocal microscope. A stack projection 10 μm thick was used for the IHC analyses. A stack projection 3-5 μm thick was used for ICC analyses. Stacks were performed using ImageJ.

Immunoprecipitation and Western Blot

Images were analyzed using ImageJ. For co-immunoprecipitation experiments, the bound fraction was normalized to the total (bound and unbound). 'Bound' refers to the fraction of the prey recombinant protein interacting with the bait recombinant protein. 'UB' refers to unbound protein which does not get pulled down. This indicates the fraction of prey recombinant protein still found in the lysate after incubation with the bait protein. Even if an interaction between recombinant proteins is found, the bait and prey recombinants protein can still also be found in the unbound fraction, since they are produced in excess. For each experiment shown the bait is specified in the figure (e.g., 'IP: anti-Flag' above the blot refers to the fact that the bait is the Flag-tagged protein). The detected prey is shown in the upper panel of blots. The graphs measure the band intensity in the western blots. The bound band of the prey protein is normalized to the total amount of protein. This is then normalized to the levels of bait protein. When comparing the

interaction between WT and mutant forms of recombinant proteins, we considered the interaction between WT recombinant proteins as the baseline (this was hence set to 1). Therefore, the quantifications concerning mutant constructs are normalized to the values obtained for the interaction of the WT recombinant proteins.

For Gli TFs analyses, band intensity was measured and normalized to GAPDH.

Statistical Analyses

Statistical analyses were performed using GraphPad Prism and BiostaTGV (https://biostatgv.sentiweb.fr/). The specific test used in each experiment is specified in the figure legend. Data were collected and processed randomly. No data points were excluded.

DATA AND CODE AVAILABILITY

The mass spectrometry proteomics data have been deposited to the ProteomeXchange Consortium via the PRIDE (Perez-Riverol et al., 2019) partner repository with the dataset identifier PXD012714. The accession number for the mass spectrometry proteomics data reported in this paper is PRIDE: PXD012714.